

Ridwan Rahman^{1*}, Samir Dirar², Yaser Jemaa³, Marios Theofanous⁴, and
Mohammed Elshafie⁵

²Senior Lecturer in Structural Engineering, University of Birmingham, Edgbaston,
Birmingham, B15 2TT, United Kingdom

⁴Lecturer in Structural Engineering, University of Birmingham, Edgbaston, Birmingham, B15 2TT, United Kingdom

*Corresponding author, Email: ridwan@eng.unri.ac.id

Abstract

Shear-deficient reinforced concrete (RC) beam-column joints (BCJs) represent one of the main factors behind the seismic damage suffered by existing concrete infrastructure, as well as the associated loss of life. This study presents a novel technique for strengthening shear-deficient RC BCJs. The technique involves embedding carbon fiber reinforced polymer (CFRP) or steel bars into epoxy-filled holes drilled within the joint core. Six exterior RC BCJs were constructed and tested under displacement-controlled cyclic loading. Five specimens, of which four were strengthened with embedded bars, were designed with shear-deficient joints according to the pre-1980s building codes. The remaining specimen was adequately designed according to ACI 352R-02. The test parameters are the type (steel or CFRP) and number (4 or 8 bars) of embedded bars. The unstrengthened control specimen experienced joint shear failure in the form of cross-diagonal cracks. The strengthened specimens, namely those strengthened with embedded steel bars, exhibited less brittle failure where damage occurred in the beam region at the early stages of loading, suggesting the outset of a beam hinge mechanism. Additionally, the strengthened specimens exhibited enhancements in joint shear strength, ductility, dissipated energy and stiffness of 6-21%, 6-93%, 10-54% and 2-35%, respectively, compared to the control specimen. This paper also presents a mechanics-based design model for RC BCJs strengthened with embedded bars. The proposed model covers all possible failure modes including yielding of the existing steel reinforcement, concrete crushing and debonding of the embedded bars. The accuracy of the proposed model was checked against the test results. The model gave good predictions with an average predicted-to-experimental ratio of 1.05 and a standard deviation of 0.04.

Keywords: Analysis; Beam-column joints; Design; Embedded bars; Fiber reinforced polymer; Reinforced Concrete; Shear strengthening

Introduction

Recent earthquakes have raised concerns about the resilience of existing reinforced concrete (RC) moment-resisting frame structures (Dolce and Goretti, 2015). In such structures, beam-column joints (BCJs) play an important role. Without proper design and detailing of the joint shear reinforcement, as the case is with the majority of the existing RC building stock designed according to the pre-1980s design codes (Bedirhanoglu et al., 2010), BCJs can be the most vulnerable elements during an earthquake and can undergo sudden brittle failure known as joint shear. This can lead to devastating effects including loss of life and severe damage to infrastructure costing billions of US dollars (González et al., 2016).

Conventional techniques for repairing and/or strengthening of shear-deficient RC BCJs include reinforced or prestressed concrete jacketing, concrete masonry unit jacketing or partial masonry infills, steel jacketing and/or addition of external steel plates (Engindeniz et al., 2005). However, these techniques suffer from the difficulty in handling heavy materials during installation and/or the need for scaffolding. Moreover, heavy materials alter the dynamic characteristics of the existing buildings and consequently careful re-analysis of the structure is usually required (Karayannis et al., 2008). Other retrofit systems for shear-deficient RC BCJs include post-tensioned rods mounted diagonally across the joint region (Yurdakul et al., 2018), and nickel-titanium shape memory alloy or steel haunches (Pampanin et al., 2006; Sasmal and Nath, 2017) that connect the upper and lower sides of the beam to the top and bottom sides of the column. However, these systems require mechanical anchoring as well as access to the column and beam faces above and/or below the BCJ region.

During the past two decades, the use of fiber reinforced polymer (FRP) strengthening techniques has gained interest due to the excellent mechanical and durability properties of the FRP composites (El-Amoury and Ghobarah, 2002; Ghobarah and Said, 2002; Ghobarah and El-Amoury, 2005; Tsonos, 2008). However, experimental results have shown that FRP debonding remains the main drawback preventing the utilization of the high tensile strength of the FRPs (Antonopoulos and Triantafillou, 2003). When un-anchored externally bonded (EB) or near-surface mounted (NSM) FRP systems are used, debonding which is attributable to the low tensile strength of the concrete cover takes place at a stress level of 20-30% of the ultimate tensile strength of the FRPs (Dirar et al., 2013). On the other hand, adequately anchored FRP strengthening systems can eliminate brittle joint shear failure, have better bond performance and reduce joint stiffness degradation. Yet, the application of EB or NSM FRP strengthening systems requires laborious surface preparation as well as protection against vandalism and fire.

An important advancement in concrete shear strengthening has been the development of the deep embedment (DE) technique (Valerio et al., 2009), also known as the embedded through-section (ETS) technique (Chaallal et al., 2011). Unlike EB and NSM FRP shear strengthening systems, the DE/ETS technique relies on embedding additional shear reinforcement, in the form of steel or FRP bars, within the concrete core. For this purpose, holes are drilled into the concrete core and then injected with an adequate binder to bond embedded bars into the concrete. Experimental and numerical studies on DE/ETS-strengthened RC beams have established the effectiveness of the method (Qin et al., 2015; Qapo et al. 2016) and demonstrated its superiority over externally applied FRP shear strengthening techniques (Chaallal et al., 2011). Nonetheless, to date, there are no detailed studies on the seismic performance of shear-deficient RC BCJs strengthened with embedded bars.

98

99 For the first time, this paper extends the applicability of the DE/ETS technique to RC BCJs
100 with inadequate shear reinforcement. The tests reported in this study assess the effectiveness
101 of the DE/ETS technique at improving the seismic behavior of shear-deficient RC BCJs and
102 examine the effect of number and type (steel vs. FRP) of embedded bars. Furthermore, the
103 paper presents a mechanics-based model for predicting the shear strength of RC BCJs
104 strengthened with embedded bars. The experimental results were used to verify the accuracy
105 of the proposed analytical formulation.

106

107 **Research Significance**

108 Recent earthquakes (e.g. Nepal, 2015; Italy, 2016 and Greece/Turkey, 2017) have
109 demonstrated that poor initial design of BCJs is one of the main reasons for the seismic
110 damage suffered by existing RC infrastructure. This paper addresses this concern by
111 providing a novel and practical technique for strengthening shear-deficient RC BCJs. The
112 new strengthening technique overcomes the premature debonding failure mode associated
113 with external shear strengthening techniques. Not only does this paper identify the effect of
114 some important parameters influencing the seismic performance of strengthened RC BCJs,
115 but also it presents an accurate mechanics-based model for predicting the shear strength of
116 DE/ETS-strengthened RC BCJs.

117

118 **Experimental Program**

119 *Specimens*

120 Six exterior RC BCJ specimens were constructed. One of the specimens was adequately
121 designed according to ACI 352R-02 (2002) whilst the remaining five specimens were

designed with deficient joint shear reinforcement to represent RC BCJs built according to pre-1980s building codes. All specimens had the same dimensions and steel reinforcement configuration, as shown in Fig. 1. The number of embedded bars was varied in order to examine the effect of joint shear reinforcement ratio. The tested specimens had a three-part designation. The first part, BCJ, stands for beam-column joint. The second part explains whether a specimen was a control (CS) or strengthened (SS) specimen. The last part clarifies whether a specimen was unstrengthened (A), adequately designed (B), strengthened with steel bars (S#) or strengthened with carbon FRP (CFRP) bars (F#), where # refers to the number of embedded bars in joint core.

All beams were reinforced with 3 $\varnothing 16$ mm deformed steel bars as top and bottom longitudinal reinforcement. These bars were bent into the joint core and extended for a distance of 195 mm ($\sim 12d_b$ where d_b is the bar diameter) to represent earlier design practice in developing countries (Garcia et al., 2014). All beams had $\varnothing 8$ mm stirrups. The first stirrup was located at a distance of 50 mm from the column face; then the stirrups were spaced at 125 mm center-to-center (c/c) for the following 1000 mm of the beam length. End stirrups were spaced at 50 mm c/c (see Fig. 1) to prevent concrete failure under the applied load.

Four corner and four internal $\varnothing 16$ mm deformed steel bars were used as longitudinal reinforcement whereas $\varnothing 8$ mm stirrups were used as shear reinforcement for the columns. In the upper and lower parts of a column, the stirrup close to the beam was placed at 50 mm from the beam face (see Fig. 1) and the consecutive stirrups were spaced at 125 mm c/c for the following 750 mm of the column length. End stirrups were spaced at 50 mm c/c at both column ends to provide additional confinement for the concrete at the loading and support points. The adequately designed specimen BCJ-CS-B had five $\varnothing 8$ mm stirrups in the joint

core whereas all other specimens had one horizontal closed stirrup in the joint core. Details of the BCJ specimens are listed in Table 1.

Materials

The test specimens were constructed using normal weight concrete with a target cylinder compressive strength of 30 MPa. The mix proportions of cement: sand: coarse aggregate for all batches were 1.0: 2.5: 3.0 and the water/cement ratio (w/c) was 0.42. The specimens were cast in a horizontal position and were mechanically vibrated to eliminate voids. They were cured for seven days in the formwork and then stored at room temperature (about 15° C). Polyethylene sheets were used to cover the wet burlap to retain moisture. Table 2 gives the average concrete compressive (f_c) and tensile (f_{ct}) strengths on the day of testing. Except for BCJ-SS-S4, all specimens had concrete compressive strength values ranging from 25 MPa to 32 MPa. The average and standard deviation values for the concrete compressive strength of these specimens were 29.8 MPa and 2.9 MPa, respectively. This is very close to the target compressive strength value of 30 MPa.

Two sizes (8 and 16 mm) of grade B500B deformed steel bars were used as longitudinal and transverse reinforcement or embedded bars. The average values of the yield strength (f_y), ultimate strength (f_u) and elastic modulus (E_s) of the steel bars obtained from three tests on each bar size are given in Table 3.

CFRP bars, with a nominal diameter of 8 mm and a nominal cross-sectional area of 50.2 mm², were used as embedded shear reinforcement. The CFRP bars had a tensile strength and elastic modulus of 2300 MPa and 130 GPa, respectively, as declared by the manufacturer. The epoxy resin used for bonding the embedded CFRP and steel bars to the concrete had a

compressive strength, tensile strength, elastic modulus and bond strength of 82.7 MPa, 43.5 MPa, 1493 MPa and 12.4 MPa, respectively, as certified by the manufacturer.

Strengthening application

In order to install the embedded bars, holes were made within the joint core by installing 10 mm acrylic rods at the required positions within the joint reinforcement cage before casting the concrete (see Fig. 2). The acrylic rods were removed from the concrete one day after casting. Prior to installing the embedded bars, the holes were enlarged using a 12 mm drilling bit and then cleaned by a wire brush and compressed air to remove any cement or aggregate residues. This procedure was also used to ensure that the holes had rough surfaces and consequently allow for better bond performance between the concrete and the embedded bars. The epoxy adhesive was used to fill two thirds of the holes. The bars were then covered with a thin layer of the adhesive and inserted into the holes. Any excess epoxy was removed. Valerio et al. (2009) demonstrated that it was possible to install embedded bars by drilling holes. Cast-in-concrete holes were used in this study for simplicity. Of note is that, in the case of interior BCJ, the presence of built-in edge beams and slabs makes it difficult to insert horizontally embedded bars into the BCJ core. However, it is still possible to insert the embedded bars into diagonally drilled holes.

Test setup

The test rig comprised two separate frames. One reaction frame was used to resist the axial load applied on the column whereas the other reaction frame was used to resist the cyclic load applied at the beam end. The upper and lower column ends were allowed to rotate in plane but lateral movements of these ends were prevented (See Fig. 3). A constant axial load of 150 kN was applied on the column using a hydraulic jack. This load represents the gravity

load that acts on the column from upper floors and corresponds to an axial load ratio of about 8%. This value was based on comparable values used by Antonopoulos and Triantafillou (2003) and Pantelides et al. (2002). The reason for using this value was to limit the beneficial effect of axial load on the shear strength of deficient BCJs (Antonopoulos and Triantafillou (2003); Pantelides et al. (2002)). The column load was continuously adjusted in such a way that the axial load acting on the column remained constant.

The cyclic load was applied at the beam tip using a 500 kN hydraulic actuator with ± 100 mm stroke. The loading history depicted in Fig. 4 was based on that proposed by ACI T1.1-01 (2001). The first drift ratio was selected to be within the linear elastic response range and, except for the final drift ratio associated with failure; any subsequent drift ratio was chosen to be between 125% and 150% of the previous drift ratio (ACI T1.1-01, 2001). The drift ratio is defined as:

$$\text{Drift ratio} = \frac{\delta}{L} \quad (1)$$

where δ is the vertical displacement of the beam-end and L is the distance from the loading point to the column face ($L=1300\text{mm}$).

Experimental Results and Discussion

Hysteresis response

The hysteresis response of the tested specimens is given in Fig. 5. The load-displacement response of the control specimen (BCJ-CS-A) is presented in Fig. 5(a). There was no significant stiffness degradation up to $\pm 0.75\%$ drift ratio (± 9.8 mm). Due to cracking, the specimen stiffness started to deteriorate gradually from $\pm 0.75\%$ (± 9.8 mm) to $\pm 3.00\%$ (± 39 mm) drift ratio, with rapid degradation taking place after $\pm 3.00\%$ (± 39 mm) drift ratio. The

specimen reached its maximum load carrying capacity (59 kN) at the first cycle of the 3.00% drift ratio loading step and then the load decreased rapidly.

For BCJ-SS-S4, the load-displacement response in Fig. 5(b) indicates that the specimen remained elastic up to $\pm 0.35\%$ drift ratio (± 4.6 mm), and subsequently maintained a quasi-linear cracked stiffness up to $\pm 2.00\%$ drift ratio (± 26 mm). The specimen attained its maximum load carrying capacity (70.8 kN) at 3.00% drift ratio (39 mm). Up to 3.00% drift ratio, pinching length was increasing gradually, indicating that the specimen was capable of dissipating energy. A gradual stiffness degradation took place after the specimen reached its maximum load carrying capacity.

Fig. 5(c) shows that BCJ-SS-F4 had a quasi-linear load-displacement response up to peak load. The maximum load carrying capacity (71.3 kN) was achieved at the first cycle of the 3.00% drift ratio (39 mm). The embedded CFRP bars seem to have controlled crack propagation because there was limited stiffness degradation up to the maximum load carrying capacity. From the second cycle of the $\pm 3\%$ drift ratio (± 39 mm) until the end of the test, both the load carrying capacity and stiffness significantly deteriorated.

For BCJ-SS-S8, the load-displacement response (see Fig. 5(d)) shows that there was no significant stiffness degradation up to $\pm 2.00\%$ drift ratio (± 26 mm). The specimen attained its maximum load carrying capacity (63.3 kN) at 3.00% drift ratio (39 mm). Further loading beyond 3.00% drift ratio resulted in significant reduction in both the load carrying capacity and stiffness.

For BCJ-SS-F8, the load-displacement response (Fig. 5(e)) was quasi-linear, without significant stiffness degradation, up to a drift ratio of $\pm 1.50\%$ (± 19.5 mm). The specimen reached its maximum load capacity (68.7 kN) at the first cycle of the 3.00% drift ratio. Upon further loading, both the overall stiffness and load carrying capacity deteriorated with the increase in drift ratio (displacement).

Comparable to that of the strengthened specimens, the load-displacement response of BCJ-CS-B was quasi-linear (see Fig. 5(f)), without significant stiffness degradation, up to a drift ratio of $\pm 1.50\%$ (± 19.5 mm). The specimen reached its maximum load carrying capacity (64.5 kN) at the first cycle of the 3.00% drift ratio (39 mm). A limited yield plateau can be seen in the envelope curve at this load level. Starting at $\pm 4.00\%$ drift ratio (± 52 mm) until the end of the test, pinching length increased gradually, indicating the capability of the specimen to dissipate energy. Moreover, both stiffness and strength deteriorated gradually as depicted in Fig. 5(f).

Fig. 5(g) compares the envelope curves of the tested specimens. Compared to the shear-deficient control specimen (BCJ-CS-A), the strengthened specimens had higher, or at least comparable, load and/or deformation capacity in both directions. Fig. 5(g) shows that the experimental response of the tested specimens under positive and negative loading was asymmetric. This is attributable to the fact that loading in a given direction can accumulate damage that affects the response in the opposite direction.

Damage evolution and failure mode

The typical crack patterns at peak load are illustrated in Fig. 6 while Fig. 7 quantifies the evolution of damage with drift ratio. The damage index (DI) method (Park and Ang, 1985;

Park et al.; 1987) together with the corresponding DIs boundaries (Varum, 2003) were used to quantify damage in the test specimens. At a given drift ratio, the strengthened specimens had lower DI values than the control specimen (BCJ-CS-A). The control specimen reached a DI of 1.0 (nominally corresponding to collapse) at a drift ratio slightly higher than 2.00% whereas the strengthened specimens reached the same DI value at a drift ratio of 3.00% to 3.60%. The adequately designed specimen (BCJ-CS-B) had the least damage evolution and approached collapse ($DI = 1.0$) at a drift ratio of about 4.00%.

The control specimen (BCJ-CS-A) experienced hybrid local damage in the form of shear cracks in the joint and flexural cracks in the beam. The failure mechanism was characterized by shear damage in the form of cross-diagonal cracks. As a result, a wide concrete wedge developed, leading to the spalling of the outer face of the concrete column after a drift ratio of 3.00%, which is typical of joint shear (JS) failure. This can be attributable to the inadequate shear reinforcement in the joint region. Compared to the control specimen, all strengthened specimens exhibited more enhanced behavior. Damage occurred in the beam region at the early stages of loading, suggesting the outset of a beam hinge (BH) mechanism, and then diagonal cracks propagated into the joint after 1.00% drift ratio. Stable hysteresis behavior with high energy dissipation capacity was also maintained until the end of the test (see Figs. 5(a) to 5(f)).

Strain response of the embedded bars

Fig. 8 depicts the envelope curves of load versus strain in the embedded bars, with tensile strain assigned a negative sign. Unfortunately, some strain gauges failed during testing and their results were discarded.

The embedded bars exhibited two stages of response during loading. In the first stage, the embedded bars were inactive prior to joint cracking and therefore did not contribute to the shear strength. The second stage is marked by the formation of inclined cracks at a load of approximately 20 kN to 35 kN. After the formation of inclined cracks, the shear links developed strain with increasing load until failure. As can be seen in Fig. 8, none of the embedded steel bars attained the yield strain of 0.29%.

The effect of type of embedded bar on strain response may be inferred by comparing the results of Group B specimens (BCJ-SS-F4 and BCJ-SS-S4). As can be seen in Fig. 8, the embedded CFRP bars were generally more strained than the embedded steel bars. This may be explained by the lower elastic modulus of the CFRP bars (130 GPa) compared with that of the steel bars (199 GPa). Fig. 8 also shows that, regardless of embedded bar type, the strain in the embedded bars of Group C specimens (BCJ-SS-F8 and BCJ-SS-S8) was generally less than that in the embedded bars of Group B specimens (BCJ-SS-F4 and BCJ-SS-S4). This was to be expected as increasing the number of bars from 4 to 8 bars results in a more distributed strain field in the joint panel and consequently less strain in the embedded bars.

Strength

The significant contribution of the embedded bars can be seen in Table 4. All strengthened specimens performed better, in terms of joint shear strength and dissipated energy, compared to BCJ-CS-A. This result demonstrates the potential of the strengthening technique. A substantial improvement in the global performance of BCJ-SS-S4 and BCJ-SS-F4 can be seen in the joint shear stress at peak load, which for both specimens increased by 6% and 21%, respectively, for the case of upward loading. Further, specimens BCJ-SS-S8 and BCJ-SS-F8 had increases of 7% and 16%, respectively, in the joint shear stress at peak load

compared to that of the control specimen (BCJ-CS-A). The strengthened specimens also showed higher joint shear strength than that of the adequately designed specimen BCJ-CS-B. For example, during upward loading, BCJ-SS-F4 and BCJ-SS-F8 had joint shear stress at peak load that was 11% and 7%, respectively, higher than that of BCJ-CS-B.

Fig. 9 presents the variation of normalized principal tensile stress with joint shear deformation. Compared to the control specimen (BCJ-CS-A), the strengthened specimens had higher cracked joint stiffness during upward (positive) loading. An exception was BCJ-SS-S4 which underwent initial joint cracking and achieved its maximum capacity during the downward (negative) loading direction. Moreover, the normalized principal tensile stress of the strengthened specimens at peak load was higher than that of the control specimen. For example, BCJ-SS-F4 had a normalized principal tensile stress at peak load that was 25% higher than that of the control specimen. The corresponding increases for BCJ-SS-S8 and BCJ-SS-F8 were 22% and 18%, respectively. This further demonstrates the potential of the proposed strengthening technique.

Ductility

The displacement ductility μ is defined as Δ_u/Δ_y , where Δ_u is the beam tip displacement at the load step corresponding to 20% reduction in ultimate load and Δ_y is the yield displacement as defined by the Equivalent Energy Elastic-Plastic curve (Park, 1989). The embedded bars enhance ductility by controlling crack width, thereby delaying the brittle shear failure of the joint panel (Li and Mobasher, 1998). Table 4 shows that the strengthened specimens generally had higher displacement ductility than that of BCJ-CS-A. A 39% (upward direction) and 93% (downward direction) increase in the displacement ductility of BCJ-SS-S4 was observed compared to that of BCJ-CS-A. The corresponding increases at upward

loading for specimens BCJ-SS-F4 and BCJ-SS-F8 were 6% and 22%, respectively; while the increases at downward loading for specimens BCJ-SS-F4, BCJ-SS-S8 and BCJ-SS-F8 were 27%, 20% and 13%, respectively. These results show that, at least for the case of downward loading, the steel-strengthened specimens had higher displacement ductility than that of the CFRP-strengthened specimens. This result can be explained by the fact that steel bars are ductile by nature whereas CFRP bars exhibit linear elastic behavior up to failure. Of note is that no displacement ductility enhancement was observed during upward loading of BCJ-SS-S8. Damage accumulation in the joint prevented the increase in the displacement ductility for the case of upward loading of BCJ-SS-S8. The premature damage and limited ductility of BCJ-SS-S8 can be further explained by the relatively low concrete strength (25 MPa) of this specimen.

Specimen BCJ-CS-B, as expected, had superior displacement ductility compared to those of the strengthened specimens. The joint shear reinforcement of BCJ-CS-B was designed according to ACI 352R-02 (2002) and aimed at satisfying both strength and ductility requirements. The displacement ductility for specimens BCJ-SS-S4, BCJ-SS-F4, BCJ-SS-S8 and BCJ-SS-F8 were 24%, 42%, 48% and 33%, respectively, less than that of BCJ-CS-B.

Energy dissipation and stiffness degradation

As depicted in Fig. 10, the energy dissipation levels achieved by the strengthened specimens were generally higher than that achieved by the control specimen, especially at drift levels of 1.00% or more. For example, the energy absorbed by the strengthened specimens at 4.00% drift ratio was 14947 kN-mm (BCJ-SS-S4), 11433 kN-mm (BCJ-SS-F4), 10616 kN-mm (BCJ-SS-S8), and 11877 kN-mm (BCJ-SS-F8), representing increases of 54%, 18%, 10% and 23%, respectively, over the corresponding value for the control specimen (BCJ-CS-A).

The effect of number of embedded bars on energy dissipation capacity may be inferred by comparing the performance of BCJ-SS-F4 and BCJ-SS-F8. As can be seen in Fig. 10, the two specimens had comparable energy dissipation levels up to 3.00% drift ratio. Beyond this load level, BCJ-SS-F8 had higher energy dissipation capacity than that of BCJ-SS-F4 due to the increased number of embedded bars. Moreover, the energy dissipation levels of the strengthened specimens at 4% drift ratio were comparable to, or higher than, that of the adequately designed specimen BCJ-CS-B, except for BCJ-SS-S8. Again, this can be explained by the relatively low concrete strength of BCJ-SS-S8.

In general, the stiffness degradation of the strengthened specimens was slower than that of BCJ-CS-A but higher than that of BCJ-CS-B. For example, Fig. 11 shows that at 4.00% drift ratio, the normalized peak-to-peak stiffness of BCJ-SS-S4, BCJ-SS-F4, BCJ-SS-S8 and BCJ-SS-F8 was 35%, 2%, 19% and 20% higher than that of BCJ-CS-A, respectively. On the other hand, the normalized peak-to-peak stiffness of BCJ-SS-S4, BCJ-SS-F4, BCJ-SS-S8 and BCJ-SS-F8 at 4.00% drift ratio was 4%, 28%, 16%, and 15% lower, respectively, than that of the adequately designed specimen BCJ-CS-B.

The effect of number of embedded bars on normalized stiffness may be inferred by comparing the performance of BCJ-SS-F4 and BCJ-SS-F8. As can be seen in Fig. 11, the two specimens had similar normalized stiffness up to 1.50% drift ratio. Beyond this load level, BCJ-SS-F8 had higher normalized stiffness values due to the increased number of embedded bars which were more effective in controlling crack opening and limiting deflection. The performance of BCJ-SS-S8 and BCJ-SS-F8 suggest that the embedded bar type has limited effect, if any, on normalized stiffness.

Beam fixed-end rotation

Fig. 12 presents the envelope curves of the normalized load versus fixed-end beam rotation for the tested specimens. The control specimen showed limited beam rotation while the specimens strengthened with embedded steel bars showed more enhanced fixed-end beam rotation than the specimens strengthened with embedded CFRP bars. The beam rotation of BCJ-CS-A at maximum load was 0.0066 radians, while the beam rotations of the strengthened specimens at maximum load varied from 0.0074 radians (BCJ-SS-F8) to 0.0092 radians (BCJ-SS-S4), representing increases from 12% to 40%. The relatively small beam rotation of the control specimen indicates the absence of a plastic hinge in the beam. The maximum rotations of BCJ-SS-S4 and BCJ-SS-S8 were comparable to that of specimen BCJ-CS-B, extending to around 0.03 radians at failure. This suggests the onset of a beam hinge mechanism in these specimens.

Analytical Model

An analytical model capable of predicting the shear strength of unstrengthened and strengthened RC BCJs with embedded bars was developed. The model is based on those developed by Pantazopoulou and Bonacci (1992) and Antonopoulos and Triantafillou (2002) and covers BCJ response before and after the yielding of the longitudinal and transverse steel reinforcement. Failure is defined as either concrete crushing or debonding of the embedded bars. As shown in Fig. 13, the model idealizes an exterior BCJ as a two-dimensional frame element; where the column width, column height, beam width and beam height are denoted as w_c , h_c , w_b and h_b respectively.

418 *Assumptions*

419 Fig. 14 shows the adopted joint stress equilibrium for joints with embedded bars. Shear
 420 stresses are introduced by direct member action and by bond stress-induced forces that
 421 develop along the reinforcement within the joint area (i.e. beam reinforcement, column
 422 reinforcement and the embedded steel or CFRP bars). To simplify the model formulation, the
 423 shear stress, ν , is assumed to be uniform along the joint boundaries. Additionally, to replicate
 424 real-life conditions before strengthening where the structure is subjected to its self-weight, it
 425 is assumed that a set of initial normal strain in the transverse direction (ε_{0t}) and initial shear
 426 strain (γ_0) has developed causing a small deformation in the steel bars (Antonopoulos and
 427 Triantafillou, 2002).

428 The maximum and minimum principal strains, ε_1 and ε_2 respectively, are linked to the strains
 429 in the longitudinal (l) and transverse (t) directions (see Fig. 14), ε_l and ε_t respectively, through
 430 Equation (2):

$$431 \quad \tan^2 \theta = \frac{\varepsilon_1 - \varepsilon_t}{\varepsilon_1 + \varepsilon_t} = \frac{\varepsilon_2 - \varepsilon_l}{\varepsilon_2 + \varepsilon_l} \quad (2)$$

432 where θ is the inclination (from the t -axis) of the maximum principal strain ε_1 .

433

434 By assuming that: (1) the maximum principal stress in the concrete (σ_1) cannot exceed its
 435 tensile strength, which is simply taken as zero; and (2) the direction of principal strains and
 436 stresses coincide (when the reinforcement has not yielded), the following equations can be
 437 written:

$$438 \quad \sigma_t = -\nu \tan \theta \quad (3)$$

$$439 \quad \sigma_l = \frac{-\nu}{\tan \theta} \quad (4)$$

440 where σ_t and σ_l are the average compressive stresses in the concrete in the transverse and
 441 longitudinal directions, respectively.

Finally, with $\sigma_l = 0$, the stress invariant condition states give the minimum principal stress in the concrete (σ_2):

$$\sigma_2 = \sigma_t + \sigma_l \quad (5)$$

Equations (2) to (5) were derived and employed in the work of Pantazopoulou and Bonacci (1992).

Shear strengthening model

Based on horizontal force equilibrium (see Fig. 14a), σ_t is given by Equation (6):

$$\sigma_t = -(\rho_s + \beta_t \rho_b) f_t - \rho_{Ft} f_{Ft} - \frac{N_h}{w_b h_b} \quad (6)$$

where ρ_s is the existing stirrup ratio, β_t is a factor to account for the bond conditions along the main beam reinforcement, ρ_b is the total longitudinal reinforcement ratio in the beam, f_t is the average stress in the horizontal stirrups (at mid-width of the joint), ρ_{Ft} is the steel or CFRP embedded reinforcement ratio in the transverse direction, f_{Ft} is the average normal stress in the steel or CFRP embedded bars at mid-width of the joint and N_h is the axial compressive force, if any, acting on the beam (usually N_h may be taken as zero).

In a similar manner, vertical force equilibrium (see Fig. 14b) dictates that:

$$\sigma_l = -(\rho_{c,in} + \beta_l \rho_c) f_l - \frac{N_v}{h_c w_c} \quad (7)$$

where $\rho_{c,in}$ is the total longitudinal reinforcement ratio in the column inside the joint core, β_l is a factor to account for the bond conditions along the main column reinforcement at the boundaries of the joint core, ρ_c is the total longitudinal reinforcement ratio in the column at

the boundaries of the joint core, f_l is the average stress in the longitudinal reinforcement (at mid-width of the joint) and N_v is the axial compressive force acting on the column.

The bond condition between the reinforcement bars and the concrete is defined by the factors β_t and β_l . For a perfect bond condition, the bond factors are taken as zero; while for negligible bond resistance the bond factors are set equal to 1.0. In an actual condition, the magnitudes of the bond factors could be between these two values (Pantazopoulou and Bonacci, 1992).

Simplifications are made, as follows, to reduce the number of variables in the problem.

$$\rho_t = \rho_s + \beta_t \rho_b \quad (8a)$$

and

$$\rho_l = \rho_{c,in} + \beta_l \rho_c \quad (8b)$$

where ρ_t and ρ_l are the effective transverse and longitudinal reinforcement ratios, respectively.

Based on the stress state in the steel reinforcement, four scenarios are considered, namely: a) before the yielding of the transverse and longitudinal reinforcement; b) after the yielding of the transverse reinforcement but before the yielding of the longitudinal reinforcement; c) after the yielding of both the transverse and longitudinal reinforcement and d) after the yielding of the longitudinal reinforcement but before the yielding of the transverse reinforcement. For each scenario, concrete crushing and debonding of the embedded bars are checked as explained in the solution procedure.

Step (a) Before the yielding of the transverse and longitudinal reinforcement

Equation (2) is rewritten by substituting ε_2 by σ_2/E_c , where E_c is the secant elastic modulus of concrete.

$$\tan^2 \theta = \left(\frac{\sigma_2 - E_c \varepsilon_l}{\sigma_2 - E_c \varepsilon_t} \right) \quad (9)$$

Next, the minimum principal stress in the concrete (σ_2) is written in terms of ν and $\tan \theta$ using Equations (3)-(5).

$$\sigma_2 = -\nu \tan \theta - \frac{\nu}{\tan \theta} = -\nu \left(\frac{\tan^2 \theta + 1}{\tan \theta} \right) \quad (10)$$

Subsequently, substituting Equations (3) and (8a) together with $f_t = E_s \varepsilon_t$, and $f_{FT} = E_f(\varepsilon_t - \varepsilon_{0t})$ (where E_s and E_f are the elastic moduli of steel and FRP, respectively) into Equation (6) yields:

$$\nu = \frac{1}{\tan \theta} (\rho_t E_s \varepsilon_t + \rho_{Ft} E_f \varepsilon_t - \rho_{Ft} E_f \varepsilon_{0t}) \quad (11a)$$

Note that N_h is taken as zero. Similarly, substituting Equations (4) and (8b) together with $f_l = E_s \varepsilon_l$ into Equation (7) yields:

$$\nu = \tan \theta \left(\rho_l E_s \varepsilon_l + \frac{N_v}{h_c w_c} \right) = \tan \theta (\rho_l E_s \varepsilon_l + e_v E_c) \quad (11b)$$

502

Equations (9)-(11) lead to a quadratic polynomial of $\tan^2 \theta$:

$$(n_{sc} \rho_l \psi + K) \tan^4 \theta + e_v \tan^2 \theta - \psi (n_{sc} \rho_l + 1) = 0 \quad (12a)$$

Equation (12a) can be rewritten in a simple form as

$$A \tan^4 \theta + B \tan^2 \theta + C = 0 \quad (12b)$$

where

$$A = (n_{sc} \rho_l \psi + K), \quad B = e_v \quad \text{and} \quad C = -\psi (n_{sc} \rho_l + 1) \quad (12c)$$

$$K = \frac{\rho_l E_s \varepsilon_t}{\rho_t E_s + \rho_{Ft} E_f} (\rho_t + \rho_{Ft} n_{Fs}) \quad (12d)$$

$$n_{sc} = \frac{E_s}{E_c} ; n_{Fs} = \frac{E_F}{E_s} ; e_v = \frac{N_v}{h_c w_c E_c} ; \psi = \rho_t \varepsilon_t + \rho_{Ft} n_{fs} \varepsilon_t - \rho_{Ft} n_{fs} \varepsilon_{0t} \quad (12e)$$

511

512 *Step (b) After the yielding of the transverse reinforcement but before the yielding of the*
 513 *longitudinal reinforcement*

514 The analysis is conducted in a similar manner to that described in Step (a), but in this case f_t
 515 is replaced by the yield strength of the transverse reinforcement (f_{yt}). By substituting $E_s \varepsilon_t$ by
 516 f_{yt} into Equations (9)-(11), the polynomial of $\tan \theta$ can be written as:

$$\left(H + \frac{1}{n_{sc}} \varepsilon_t \right) \tan^4 \theta + \frac{1}{n_{sc} \rho_l} e_v \tan^2 \theta - H \left(\frac{1}{n_{sc} \rho_l} - 1 \right) = 0 \quad (13)$$

$$\text{where} \quad H = \rho_t \frac{f_{yt}}{E_s} + \rho_{Ft} n_{fs} \varepsilon_t - \rho_{Ft} n_{fs} \varepsilon_{0t} \quad (14)$$

519

520 *Step (c) After the yielding of both the transverse and longitudinal reinforcement*

521 The analysis is conducted in a similar manner to that described in Step (a), but in this case f_t
 522 is replaced by f_{yt} and f_l is replaced by the yield strength of the longitudinal reinforcement (f_{yl}).
 523 By substituting $E_s \varepsilon_t$ by f_{yt} and $E_s \varepsilon_l$ by f_{yl} , into Equations (9)-(11), the polynomial of $\tan \theta$ can
 524 be written as:

$$\left(H + \frac{1}{n_{sc}} \varepsilon_t \right) \tan^4 \theta - \frac{1}{n_{sc}} \frac{f_{yl}}{E_s} \tan^2 \theta - H = 0 \quad (15)$$

526 where H is given by Equation (14).

527

528

529 *Step (d) After the yielding of the longitudinal reinforcement but before the yielding of the*
 530 *transverse reinforcement*

The analysis is conducted in a similar manner to that described in Step (a), but in this case f_i is replaced by f_{yl} . By substituting $E_s \varepsilon_l$ by f_{yl} into Equations (9)-(11), the polynomial of $\tan \theta$ can be written as:

$$\left(T + \frac{E_c \rho_t \varepsilon_t + E_c \rho_{Ft} n_{Fs} \varepsilon_t}{\rho_t E_s + \rho_{Ft} E_F} \right) \tan^4 \theta - \frac{1}{n_{sc}} \left(\frac{f_{yl}}{E_s} \right) \tan^2 \theta - T = 0 \quad (16)$$

where
$$T = \rho_t \varepsilon_t + \rho_{Ft} n_{Fs} \varepsilon_t - \rho_{Ft} n_{Fs} \varepsilon_{0t} \quad (17)$$

Solution procedure

Initial inputs are required to calculate the stresses and strains in the joint up to failure. The inputs can be categorized into: (a) geometric variables (beam and column cross-sections, effective width and depth of the joint, horizontal (beam) and vertical (column) reinforcement ratios, and existing and embedded joint reinforcement ratios); (b) bond condition variables (β_t and β_l); (c) material properties (concrete strength; concrete stress-strain properties (see Equation 18); elastic moduli of the concrete, steel and FRP; yield strengths of the beam, column and joint reinforcement; and debonding properties of the embedded bars (see Equation 19)); (d) the axial force acting on the column and (e) the initial normal strain ε_{0t} .

The procedure is initiated by incrementing the transverse strain, ε_t . Prior to first yielding of the steel reinforcement, Equation (12b) is solved for $\tan \theta$ and the shear stress in the joint area is calculated using Equation (11a). At each step of the calculation, the stresses in both the transverse (beam and joint) and longitudinal (column) reinforcement are checked against their yield strengths. Post yielding of the steel reinforcement, Equations (13), (15) or (16) are activated depending on the yield sequence of the longitudinal and transverse reinforcement. The value of $\tan \theta$ is obtained by solving the equation corresponding to the active scenario in each step. Next, the normal stress in the embedded bars, along the transverse direction at the

mid-height of the joint, is evaluated. At the end of each step, two failure modes are checked:
concrete crushing and debonding of the embedded bars.

Concrete crushing occurs when σ_2 reaches the maximum concrete strength (f_c^{max}) as defined
in Equation (18) (Pantazopoulou and Bonacci, 1992).

$$\sigma_2 = f_c^{max} \left[2 \frac{\varepsilon_2}{\varepsilon_{max}} - \left(\frac{\varepsilon_2}{\varepsilon_{max}} \right)^2 \right] \quad (18.a)$$

$$\left\{ \begin{array}{l} f_c^{max} = \lambda f_c \\ \varepsilon_{max} = \lambda \varepsilon_0 \\ \lambda = \frac{1 + \rho_{sv} |f_{ys} / f_c|}{0.8 - 0.34(\varepsilon_1 / \varepsilon_0)} \end{array} \right\} \quad (18.b)$$

where ε_0 is the failure strain of concrete in uniaxial compression (taken as -0.002), ρ_{sv} is the
volume ratio of stirrups and f_{ys} is the yield stress of stirrups.

On the other hand, debonding of the embedded bars takes place when the maximum bond
strength between the concrete and the embedded bars ($\tau_{b,max}$) is exceeded. For embedded
CFRP bars, $\tau_{b,max}$ is defined by Equation (19a) (Okelo and Yuan, 2005); whereas for
embedded steel bars, $\tau_{b,max}$ is defined by Equation (19b) (CEB-FIP, 1993).

$$\tau_{b,max} = 14.7 \frac{\sqrt{f_c}}{d_b} \quad (19.a)$$

$$\tau_{b,max} = 2.0 \sqrt{(f_c - 8)} \quad (19.b)$$

Comparison between predicted and experimental results

The analytical model was used to predict the shear strength of the tested RC BCJs. Table 5 compares the predicted and experimental results. Perfect bond was assumed between the concrete and the longitudinal and transverse reinforcement, corresponding to $\beta_t = \beta_l = 0$. It is evident from Table 5 that the proposed model gives excellent results in terms of both accuracy and precision. The model had an overall average predicted-to-experimental ratio of 1.05 with a standard deviation of 0.04. The strengthened RC BCJs had predicted-to-experimental ratios ranging from 1.02 to 1.07 whereas the control specimens had predicted-to-experimental ratios ranging from 1.01 to 1.11. This result suggests that the shear strength of the strengthened specimens is better predicted by the model. It is recommended that additional tests be carried out to further evaluate the accuracy of the proposed model and expand the database of RC BCJs strengthened with embedded bars.

Conclusions

This study presents results of an experimental and analytical investigation on the structural performance of exterior RC BCJs strengthened with embedded bars. It also provides insight into the effect of type (CFRP or steel) and number (four or eight) of embedded bars on the structural behavior of the strengthened BCJs. Based on the results of this study, the following conclusions are drawn.

- All strengthened specimens experienced less damage and had an improved load and/or deformation capacity compared with the control specimen.
- Due to the lower elastic modulus of the CFRP bars compared with that of the steel bars, the embedded CFRP bars had higher strain than the corresponding steel bars. For both embedded bar types, increasing the number of bars from 4 to 8 bars reduced the strain in the embedded bars.

- The strengthened specimens exhibited enhancements in joint shear strength and normalized principal tensile stress at peak load of 6-21% and 18-25%, respectively, compared with the control specimen. The strengthened specimens also outperformed the adequately designed specimen.
- The strengthened specimens were 6-93% more ductile compared with the control specimen. Due to the ductile nature of the steel bars, the steel-strengthened specimens exhibited a more ductile behavior than the CFRP-strengthened specimens did.
- The energy dissipation capacity and peak-to-peak stiffness of the strengthened specimens were 10-54% and 2-35%, respectively, higher than those of the control specimen. Both parameters increased with the increase in the number of embedded bars. The results suggest that the type of embedded bar has insignificant effect on energy dissipation capacity and peak-to-peak stiffness.
- The control specimen had limited beam fixed-end rotation, indicating the absence of a plastic hinge in the beam. On the other hand, the strengthened specimens had much higher beam fixed-end rotation, suggesting the onset of a beam hinge mechanism. Moreover, the steel-strengthened specimens had higher beam fixed-end rotation compared with the CFRP-strengthened specimens.
- A design model is developed for RC BCJs strengthened with embedded bars. The accuracy of the proposed model is verified against the experimental results reported in this study. The proposed model showed good correlation with the experimental results, attaining an average predicted-to-experimental ratio and a standard deviation of 1.05 and 0.04, respectively.

Acknowledgements

The first author highly appreciates the financial support provided by the Directorate General of Higher Education, Ministry of Research and Higher Education of Indonesia through Grant 323/E4.4/K/2012. The authors gratefully acknowledge the support provided by the technical staff of the Structures Laboratory at the University of Birmingham.

References

- ACI 352R-02. (2002). *Recommendations for Design of Beam-Column Connections in Monolithic Reinforced Concrete Structures*, American Concrete Institute, Farmington Hills, Mich.
- ACI T1.1-01. (2001). *Acceptance Criteria for Moment Frames Based on Structural Testing*, American Concrete Institute, Farmington Hills, Mich.
- Akguzel, U., and Pampanin, S. (2012). "Assessment and Design Procedure for the Seismic Retrofit of Reinforced Concrete Beam-Column Joints using FRP Composite Materials." *ASCE Journal of Composites for Construction*, 16(1), 21-34.
- Antonopoulos, C. P., and Triantafillou, T. C. (2002). "Analysis of FRP-Strengthened RC Beam-Column Joints." *ASCE Journal of Composites for Construction*, 6(1), 41-51.
- Antonopoulos, C. P., and Triantafillou, T. C. (2003). "Experimental Investigation of FRP-Strengthened RC Beam-Column Joints." *ASCE Journal of Composites for Construction*, 7(1), 39-49.
- Bedirhanoglu, I., Ilki, A., Pujol, S., and Kumbasar, N. (2010). "Behavior of Deficient Joints with Plain Bars and Low-Strength Concrete." *ACI Structural Journal*, 107(3), 300-310.
- CEB-FIP. (1993). *CEB-FIP Model Code 1990*, Comité Euro-International du Béton, Lausanne, Switzerland.

646 Chaallal, O., Mofidi, A., Benmokrane, B., and Neale, K. (2011). "Embedded Through-
647 Section FRP Rod Method for Shear Strengthening of RC Beams: Performance and
648 Comparison with Existing Techniques." *ASCE Journal of Composites for*
649 *Construction*, 15(3), 374-383.

650 Dirar, S., Lees, J. M., and Morley, C. T. (2013). "Precracked Reinforced Concrete T-beams
651 Repaired in Shear with Prestressed Carbon Fibre-Reinforced Polymer Straps." *ACI*
652 *Structural Journal*, 110(5), 855-866.

653 Dolce, M., and Goretti, A. (2015). "Building Damage Assessment After The 2009 Abruzzi
654 Earthquake." *Bulletin of Earthquake Engineering*, 13, 2241-2264.

655 El-Amoury, T., and Ghobarah, A. (2002). "Seismic Rehabilitation of Beam-Column Joint
656 using GFRP Sheets." *Engineering Structures*, 24(11), 1397-1407.

657 Engindeniz, M., Kahn, L. F., and Zureick, A. (2005). "Repair and Strengthening of
658 Reinforced Concrete Beam-Column Joints: State of the Art." *ACI Structural Journal*,
659 102(2), 187-197.

660 Garcia, R., Jemaa, Y., Helal, Y., and Guadagnini, M. (2014). "Seismic Strengthening of
661 Severely Damaged Beam-Column RC Joints Using CFRP." *ASCE Journal of*
662 *Composites for Construction*, 18(2), 04013048.

663 Ghobarah, A., and El-Amoury, T. (2005). "Seismic Rehabilitation of Deficient Exterior
664 Concrete Frame Joints." *ASCE Journal of Composites for Construction*, 9(5), 408-
665 416.

666 Ghobarah, A., and Said, A. (2002). "Shear Strengthening of Beam-Column Joints."
667 *Engineering Structures*, 24(7), 881-888.

668 González, A. D., Dueñas-Osorio, L., Sánchez-Silva, M., and Medaglia, A. L. (2016). "The
669 Interdependent Network Design Problem for Optimal Infrastructure System
670 Restoration." *Computer-Aided Civil and Infrastructure Engineering*, 31(5), 334-350.

671 Karayannis, C. G., Chalioris, C. E., and Sirkelis, G. M. (2008). "Local Retrofit of Exterior
672 RC Beam–Column Joints using Thin RC Jackets—An Experimental Study."
673 *Earthquake Engineering & Structural Dynamics*, 37(5), 727-746.

674 Li, C. Y., and Mobasher, B. (1998). "Finite Element Simulations of Fiber Pullout Toughening
675 in Fiber Reinforced Cement Based Composites." *Advanced Cement Based Materials*,
676 7(3–4), 123--132.

677 Okelo, R., and Yuan, R. L. (2005). "Bond Strength of Fiber Reinforced Polymer Rebars in
678 Normal Strength Concrete." *ASCE Journal of Composites for Construction*, 9(3), 203-
679 213.

680 Pampanin, S., Christopoulos, C., and Chen, T. H. (2006). "Development and Validation of a
681 Metallic Haunch Seismic Retrofit Solution for Existing Under-designed RC Frame
682 Buildings." *Earthquake Engineering & Structural Dynamics*, 35(14), 1739-1766.

683 Pantazopoulou, S., and Bonacci, J. (1992). "Consideration of Questions about Beam-Column
684 Joints." *ACI Structural Journal*, 89(1), 27-36.

685 Pantelides, C. P., Clyde, C., and Reaveley, L. D. (2002). "Performance-Based Evaluation of
686 Reinforced Concrete Building Exterior Joints for Seismic Excitation." *Earthquake
687 Spectra*, 18(3), 449-480.

688 Park, R. (1989). "Evaluation of Ductility of Structures and Structural Assemblages from
689 Laboratory Testing." *Bulletin of the New Zealand National Society for Earthquake
690 Engineering*, 22(3), 155-166.

691 Park, Y. J., and Ang, A. H. S. (1985). "Mechanistic Seismic Damage Model for Reinforced
692 Concrete." *ASCE Journal of Structural Engineering*, 111(4), 722-739.

693 Park, Y. J., Ang, A. H. S., and Wen, Y. K. (1987). "Damage-Limiting Aseismic Design of
694 Buildings." *Earthquake Spectra*, 3(1), 1-26.

- Qapo, M., Dirar, S., and Jemaa, Y. (2016). "Finite Element Parametric Study of Reinforced Concrete Beams Shear-Strengthened with Embedded FRP Bars." *Composite Structures*, 149, 93-105.
- Qin, S., Dirar, S., Yang, J., Chan, A. H. C., and Elshafie, M. (2015). "CFRP Shear Strengthening of Reinforced-Concrete T-Beams with Corroded Shear Links." *ASCE Journal of Composites for Construction*, 19(5), 04014081.
- Sasmal, S., and Nath, D. (2017). "Seismic Performance of Non-invasive Single Brace Made of Steel and Shape Memory Alloy for Retrofit of Gravity Load Designed Sub-assemblages." *Engineering Structures*, 143, 316-329.
- Tsonos, A. G. (2008). "Effectiveness of CFRP-Jackets and RC-Jackets in Post-earthquake and Pre-earthquake Retrofitting of Beam-Column Subassemblages." *Engineering Structures*, 30, 777-793.
- Valerio, P., Ibell, T. J., and Darby, A. P. (2009). "Deep embedment of FRP for concrete shear strengthening." *Structures and Buildings*, 162(5), 311-321.
- Varum, H. (2003). "Seismic Assessment, Strengthening and Repair of Existing Buildings." PhD thesis, University of Aveiro, Aveiro, Portugal.
- Yurdakul, Ö., Tunaboyu, O., and Avşar, Ö. (2018). "Retrofit of Non-seismically Designed Beam-Column Joints by Post-tensioned Superelastic Shape Memory Alloy Bars." *Bulletin of Earthquake Engineering*, in press.

List of Figures

- Fig. 1. Reinforcement details of the test specimens, unit in mm.
- Fig. 2. Strengthening configuration.
- Fig. 3. Schematic drawing of the experimental set-up.
- Fig. 4. Loading history.
- Fig. 5. Load versus displacement curves.
- Fig. 6. Crack patterns of the tested specimens at peak load (corresponding to 3.00% drift ratio).
- Fig. 7. Damage versus drift ratio.
- Fig. 8. Envelope curves of load versus strain in the embedded bars.
- Fig. 9 Envelope curves of normalized principal tensile stress versus joint shear deformation
- Fig. 10. Comparison of energy dissipation.
- Fig. 11. Comparison of normalized peak-to-peak stiffness.
- Fig.12. Envelope curves of normalized load versus beam fixed-end rotation.
- Fig. 13. Idealization of an external beam-column joint, based on Akguzel and Pampanin (2012): (a) Moments and shear forces acting on the boundaries of the plane frame element; (b) Kinematics and compatibility conditions in joint region; (c) Mohr's circle for average stresses.
- Fig. 14. Stress equilibrium in a joint with embedded bars, modified after Antonopoulos and Triantafillou (2002).

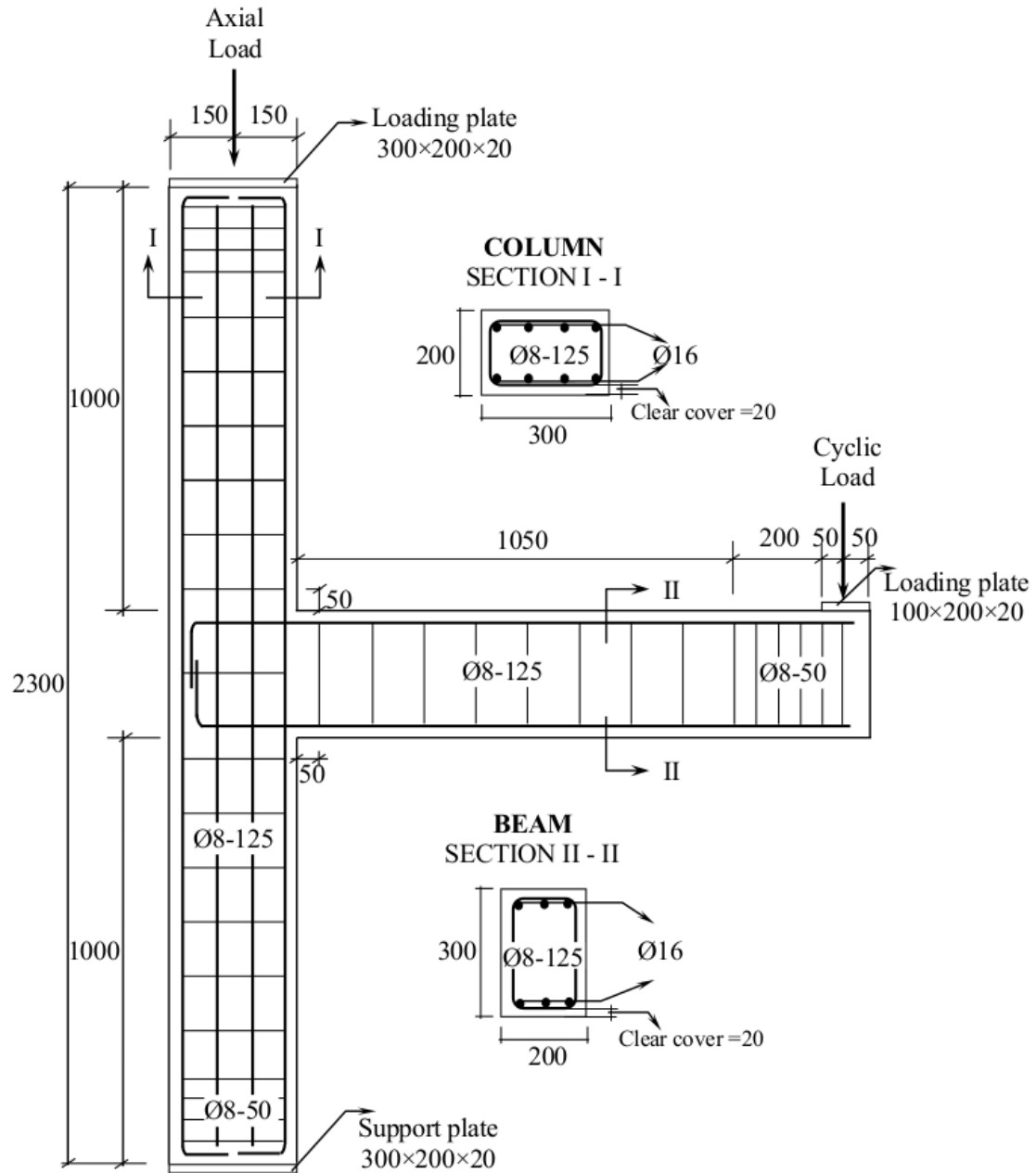
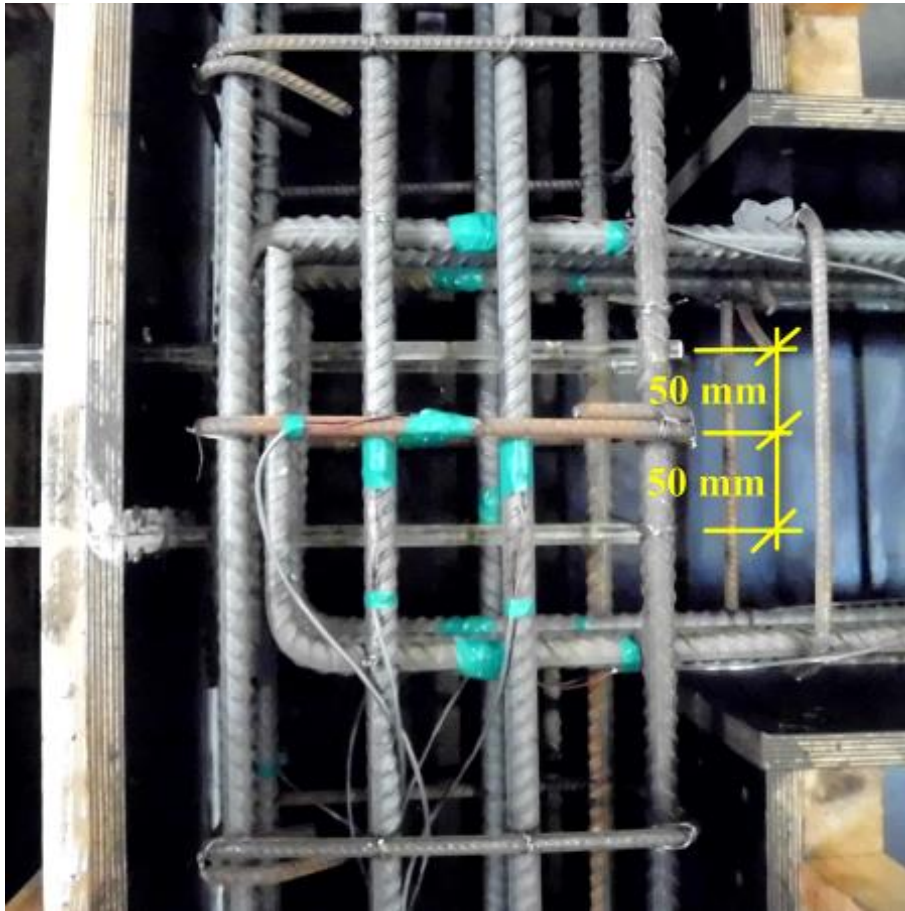
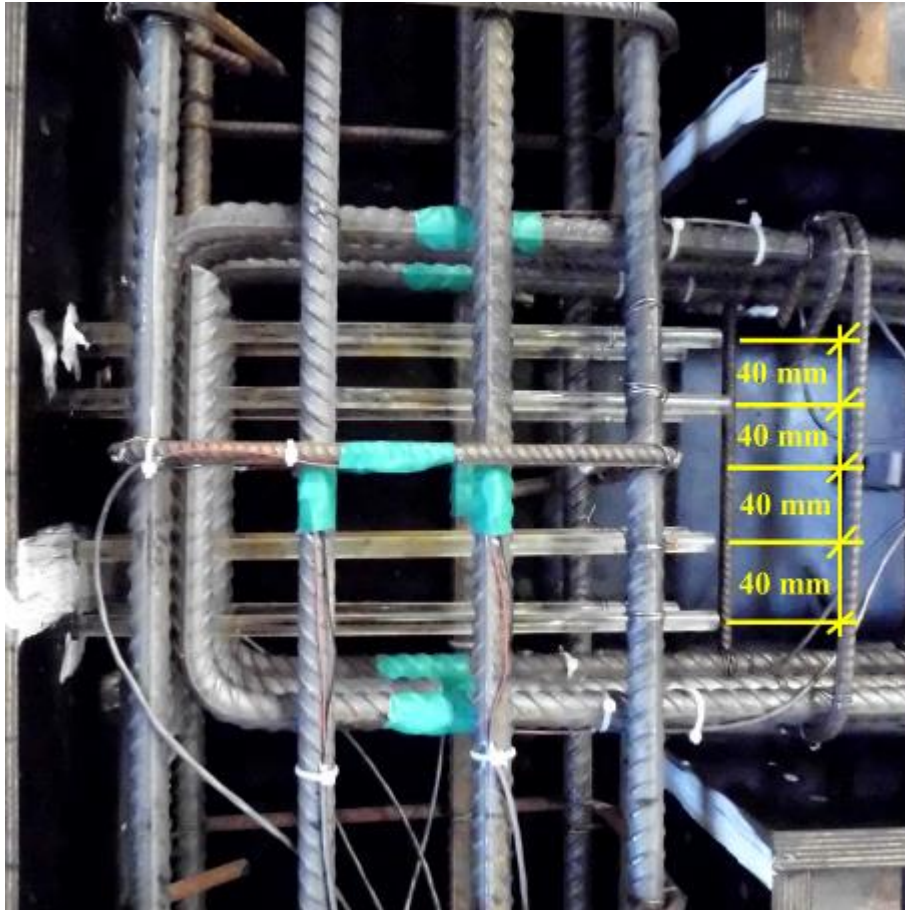


Fig. 1. Reinforcement details of the test specimens, unit in mm.

Fig. 2. Strengthening configuration.



a) Acrylic rods within specimens with four embedded bars



764

765

766 b) Acrylic rods within specimens with eight embedded bars

767

768

769

770

771

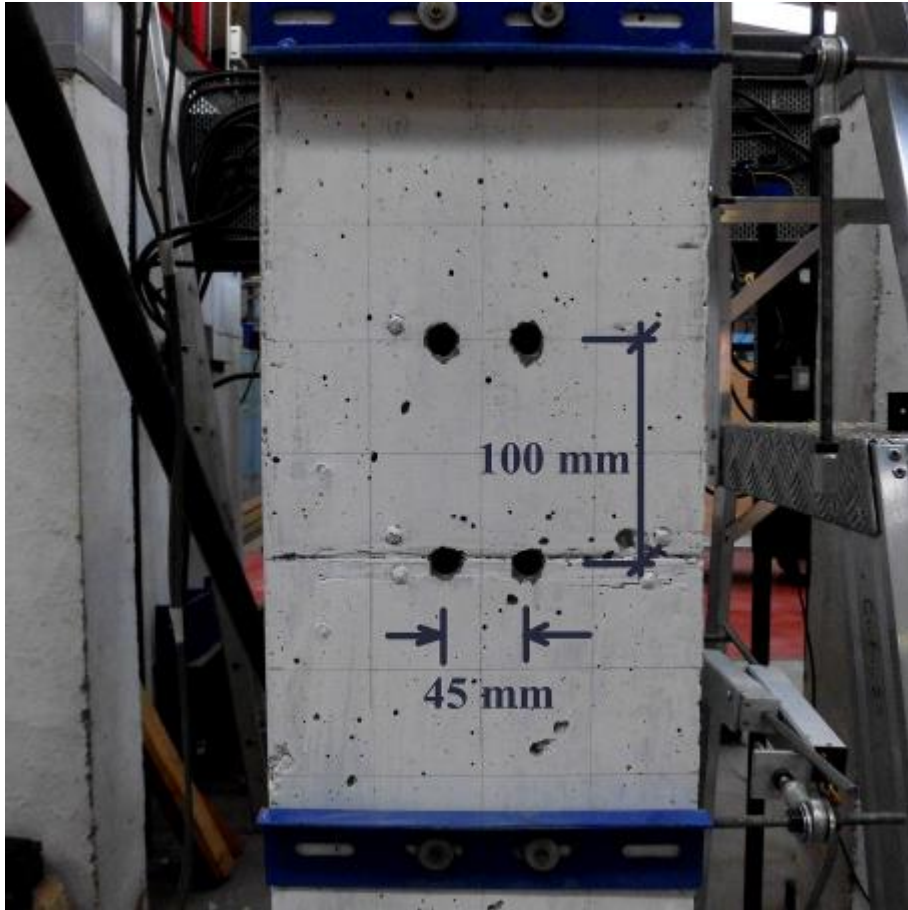
772

773

774

775

776



777

778 c) Cast-in-concrete holes

779

780

781

782

783

784

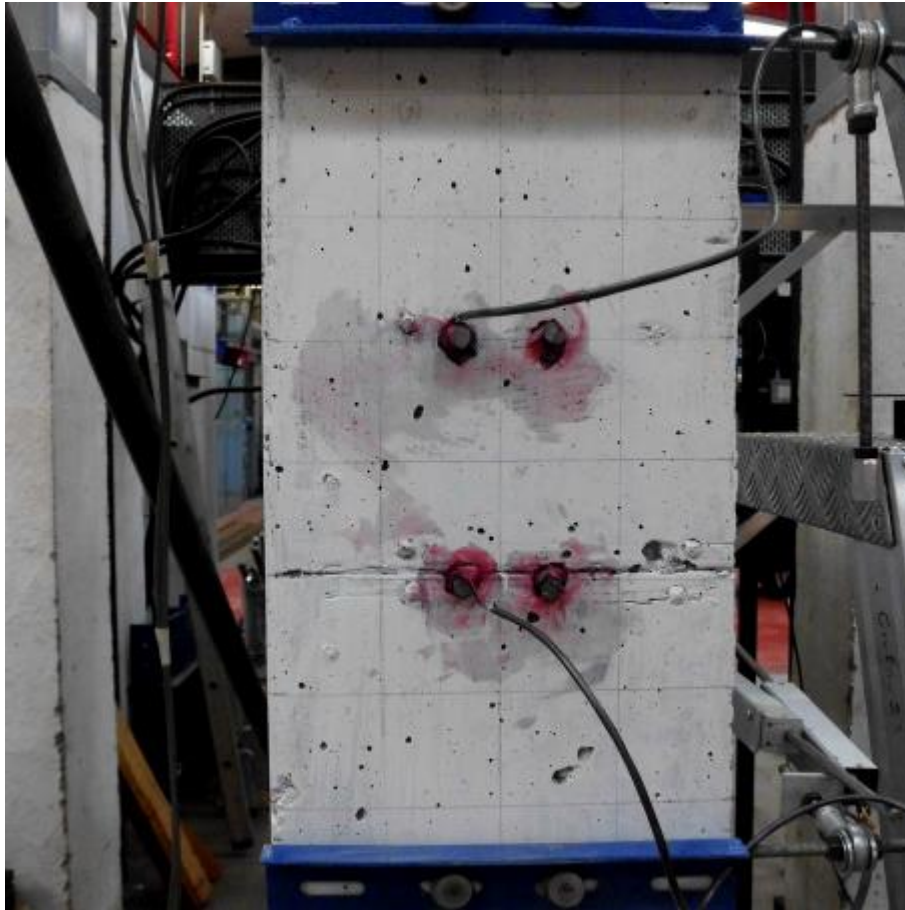
785

786

787

788

789



790

791

792 d) Application of embedded bars

793

794

795

796

797

798

799

800

801

802

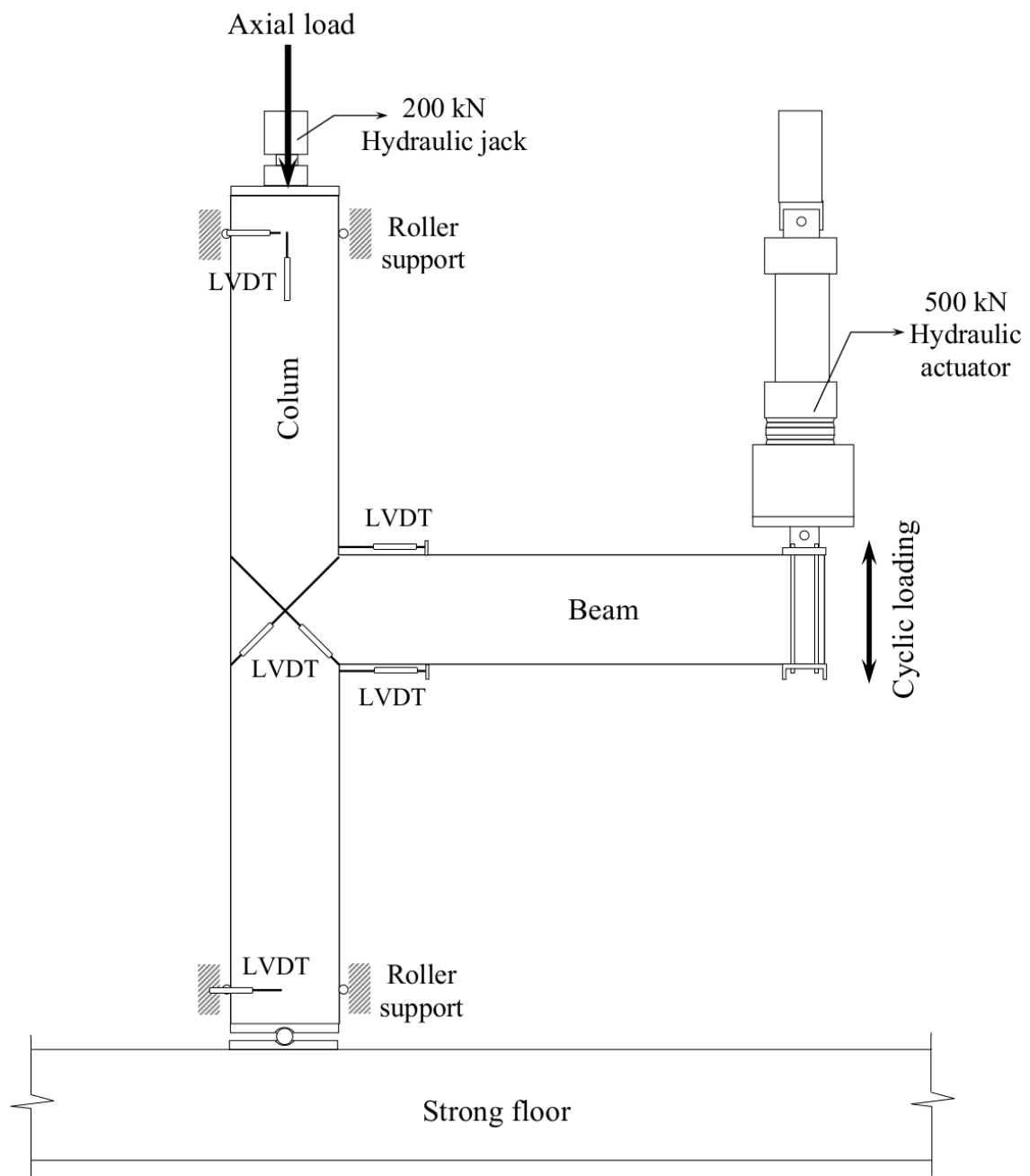


Fig. 3. Schematic drawing of the experimental set-up.

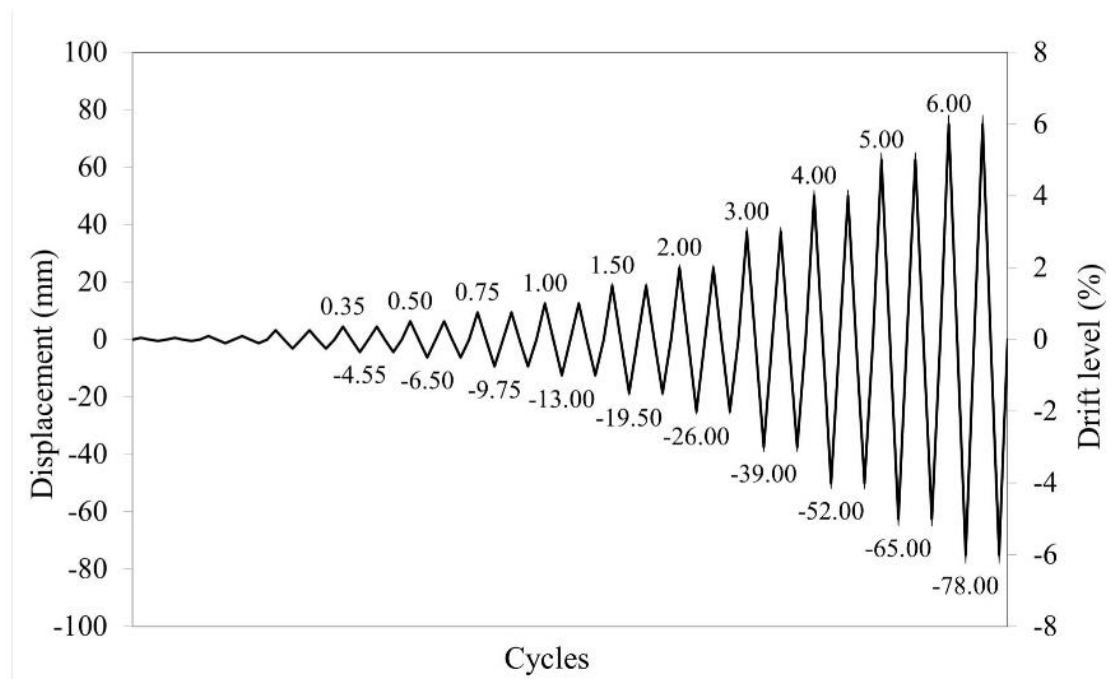
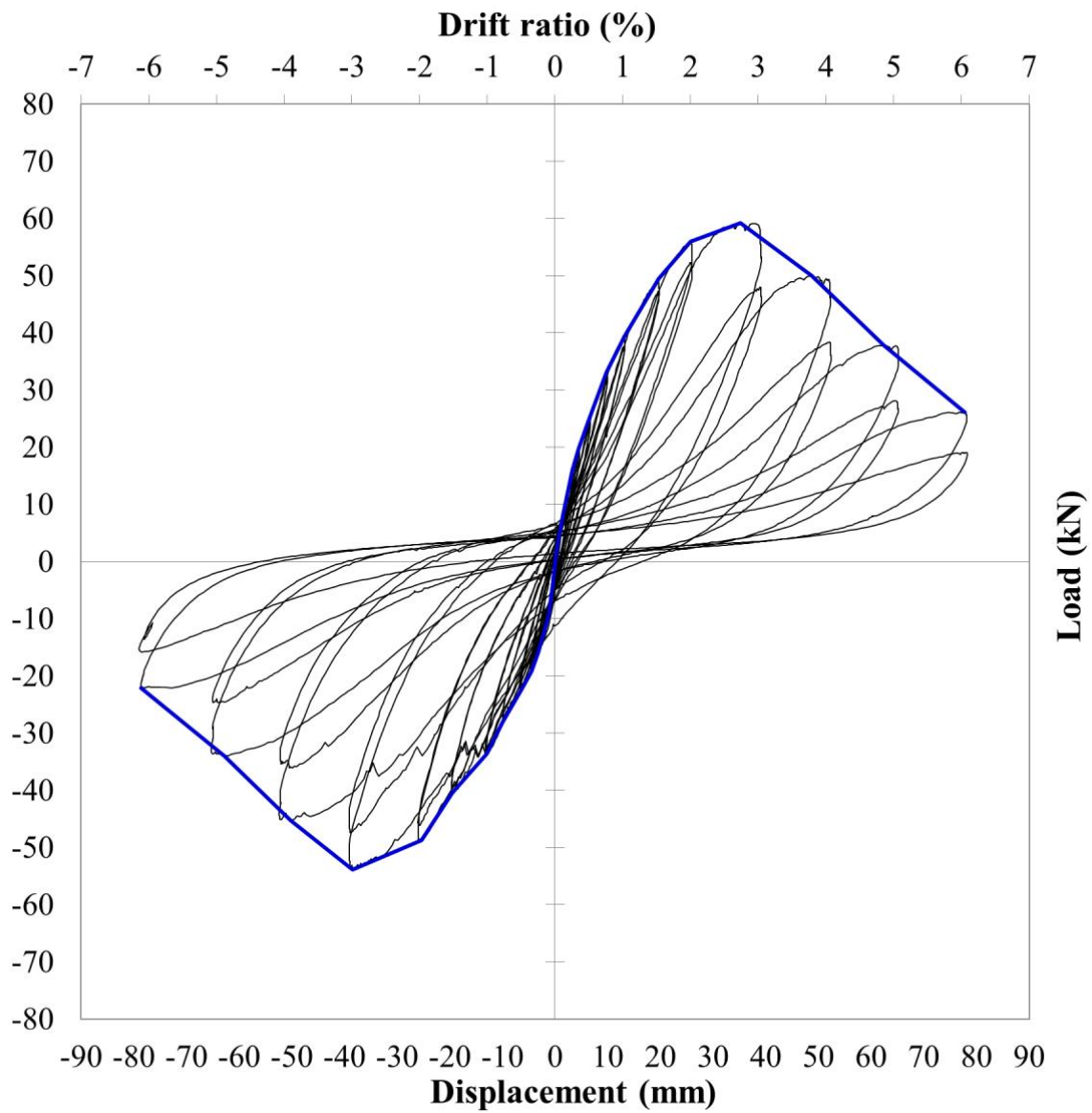


Fig. 4. Loading history.

825 **Fig. 5.** Load versus displacement curves.



826

827 (a) BCJ-CS-A

828

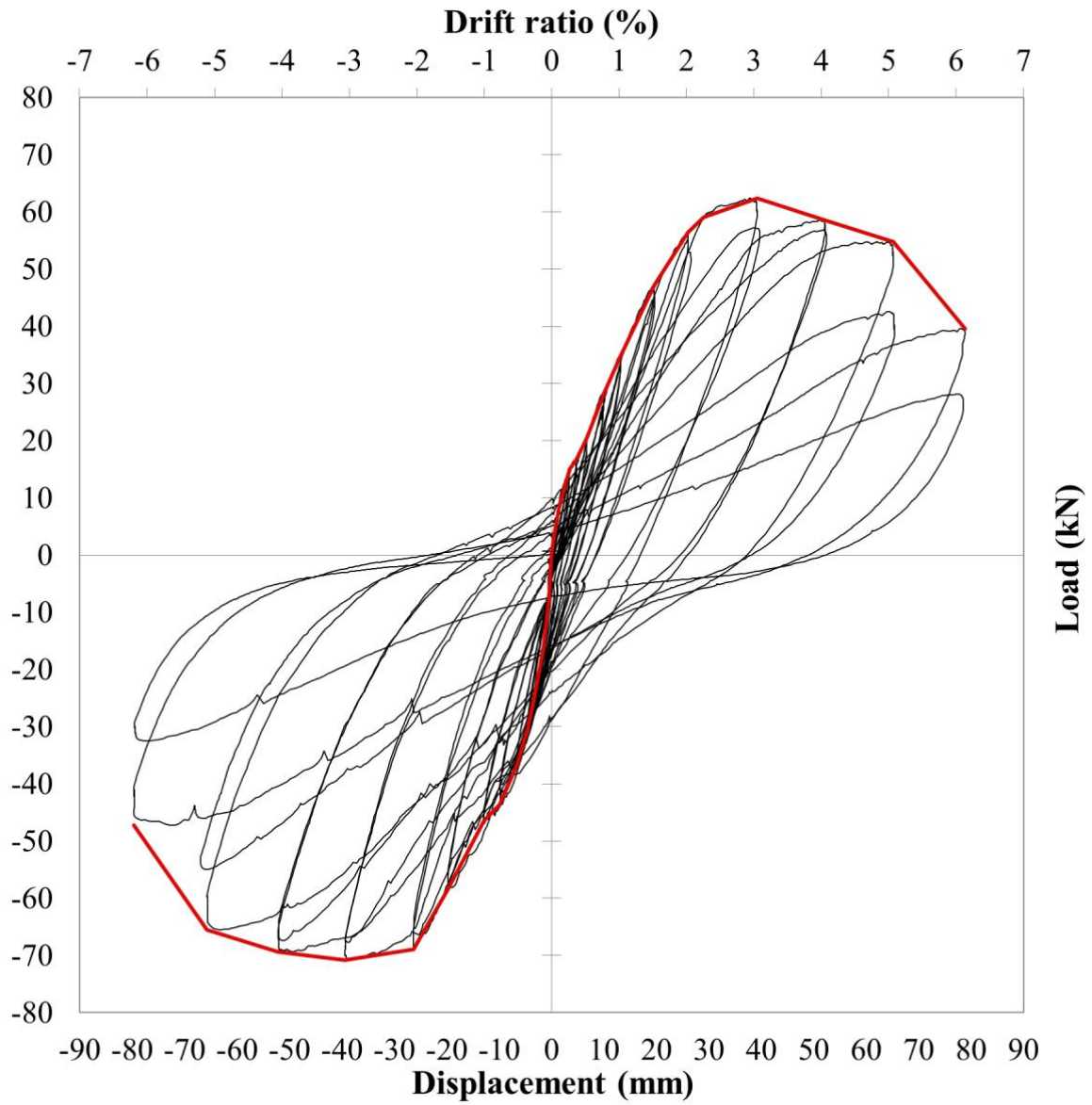
829

830

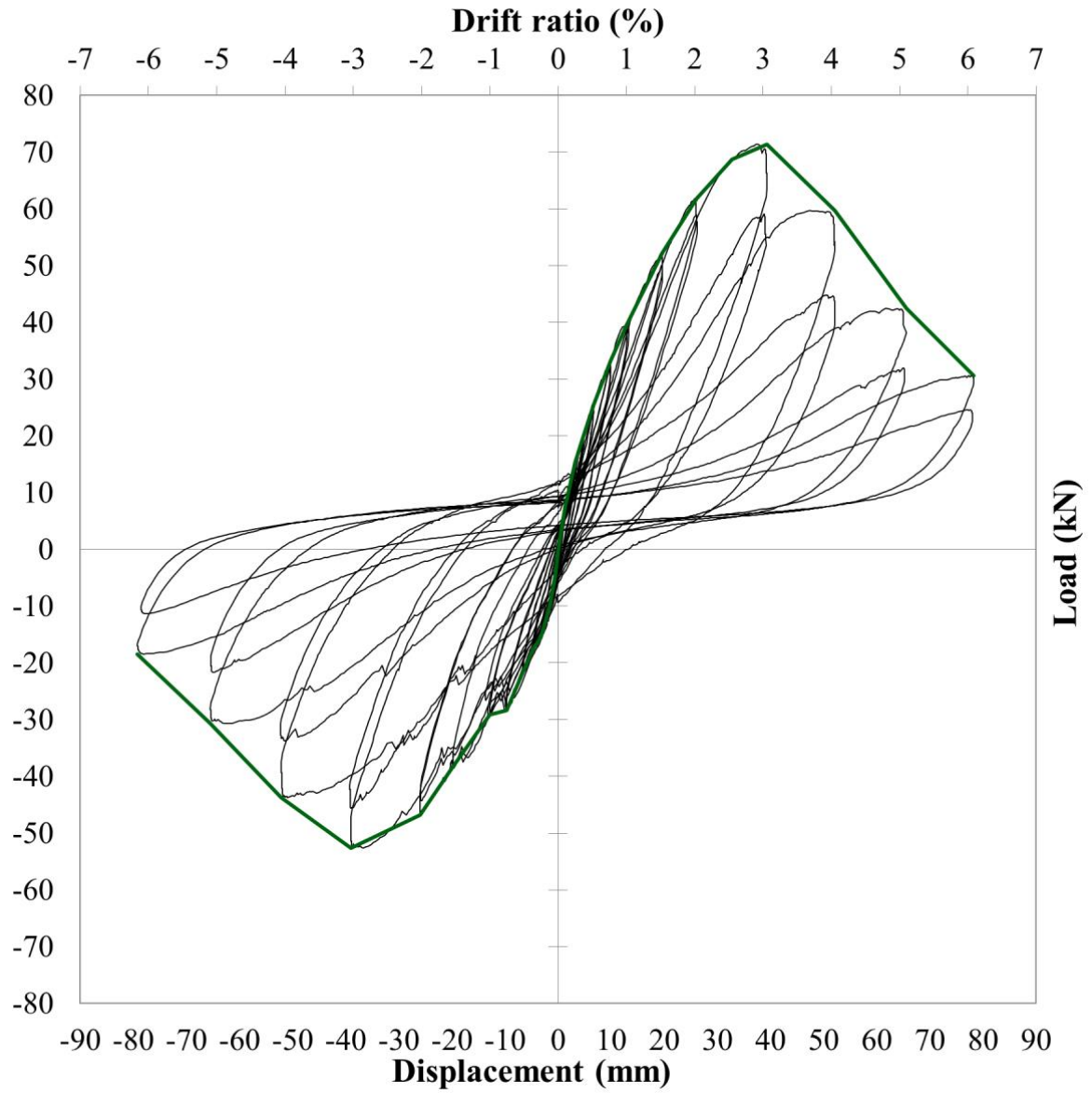
831

832

833



(b) BCJ-SS-S4



843

844 (c) BCJ-SS-F4

845

846

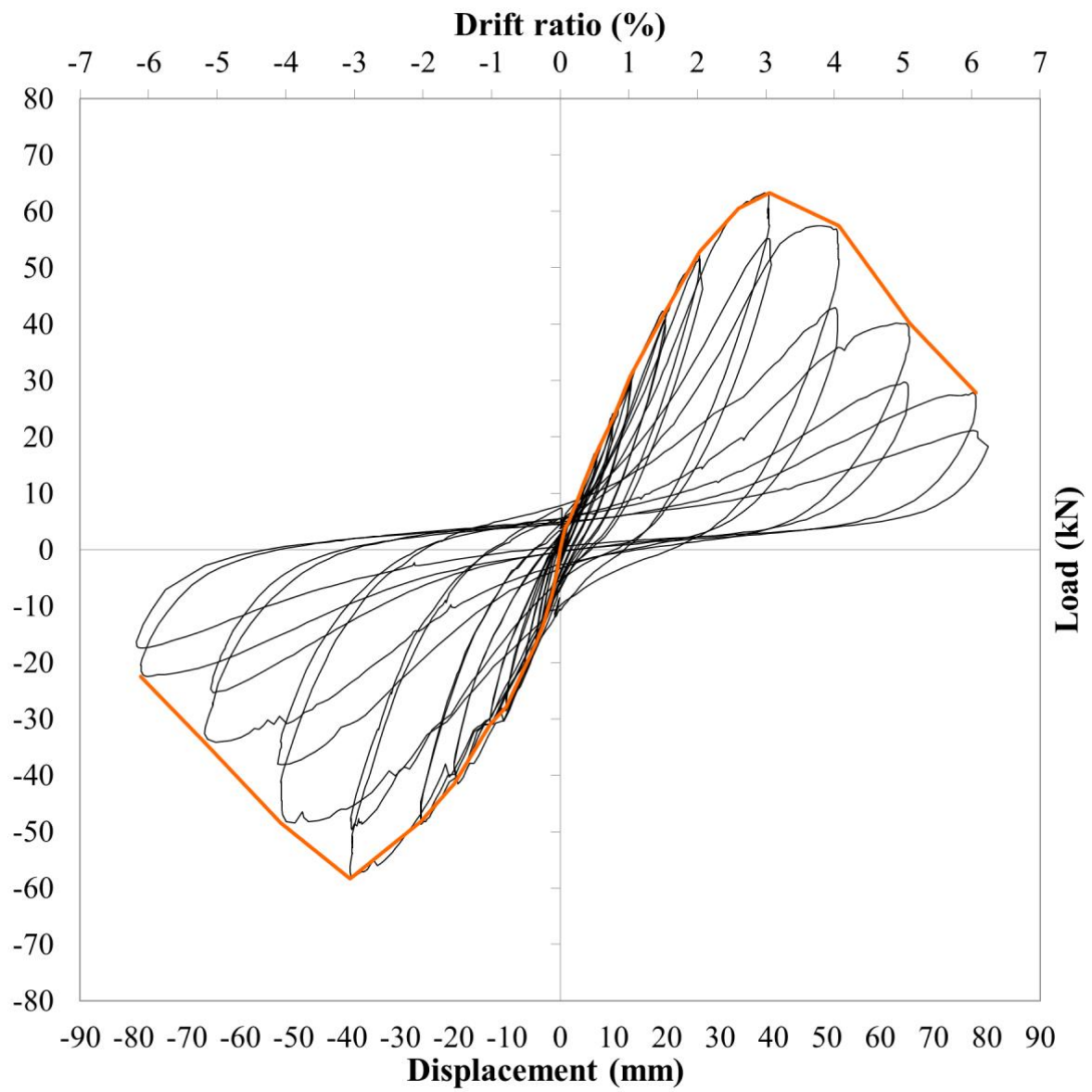
847

848

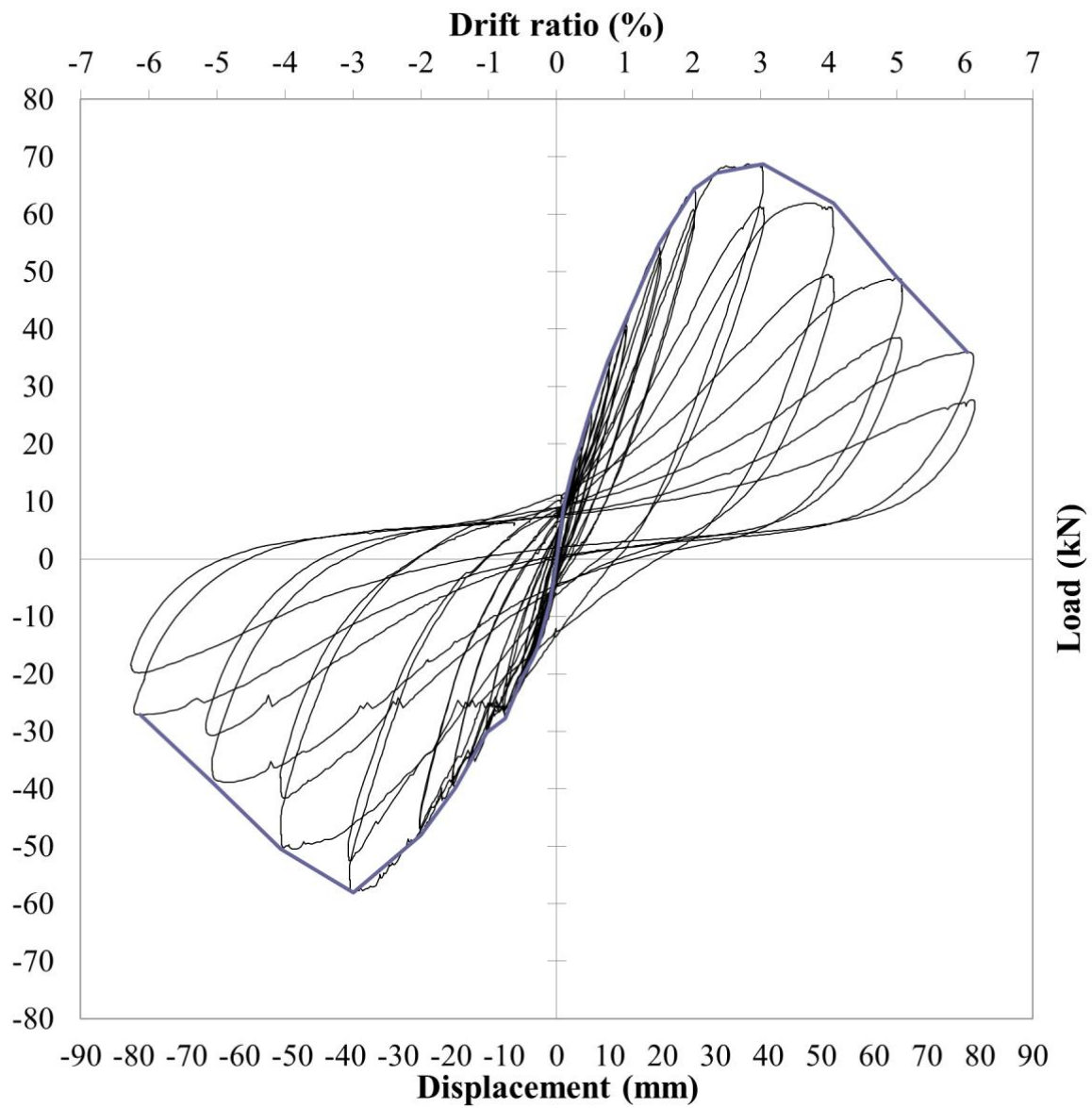
849

850

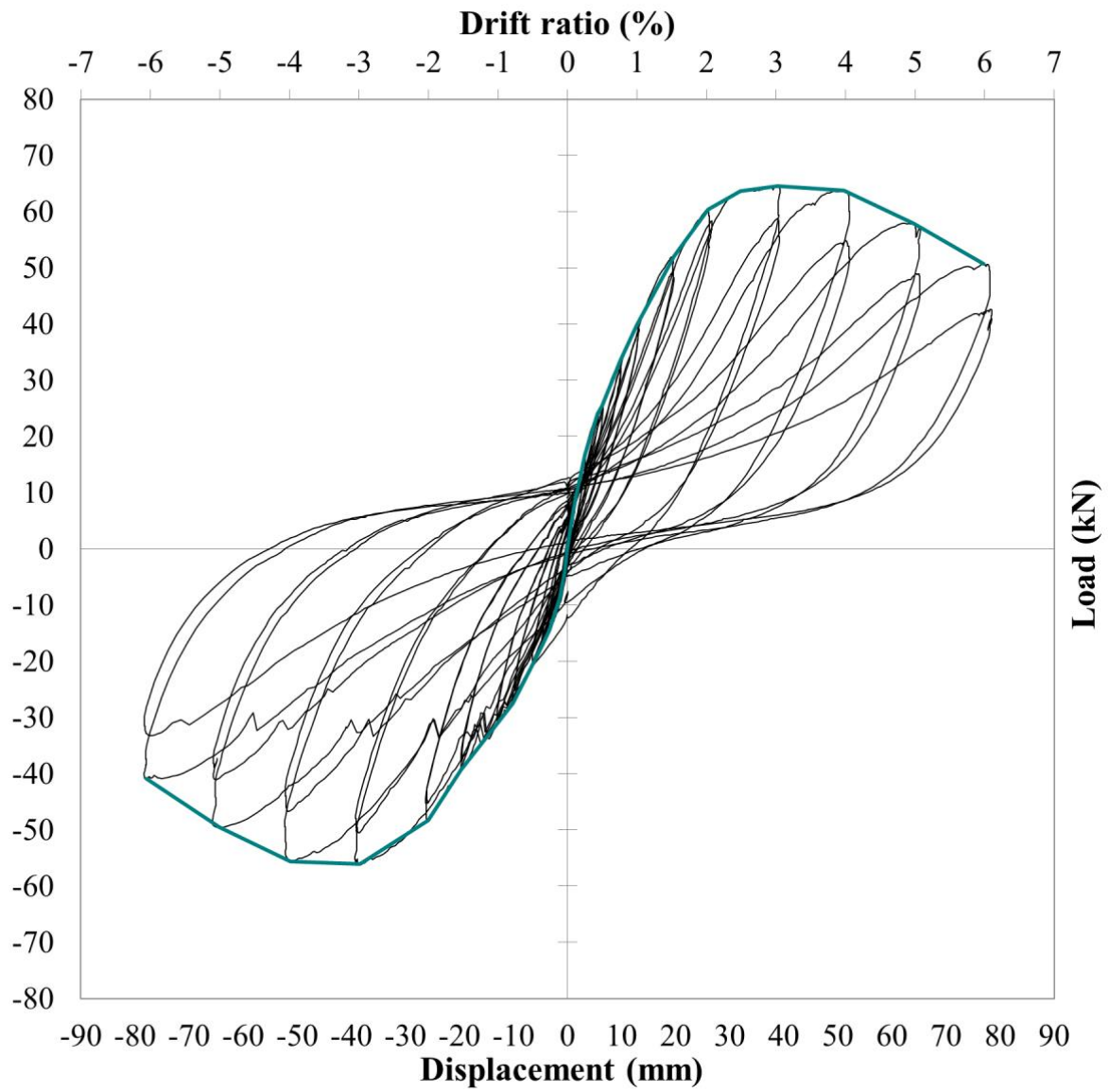
851



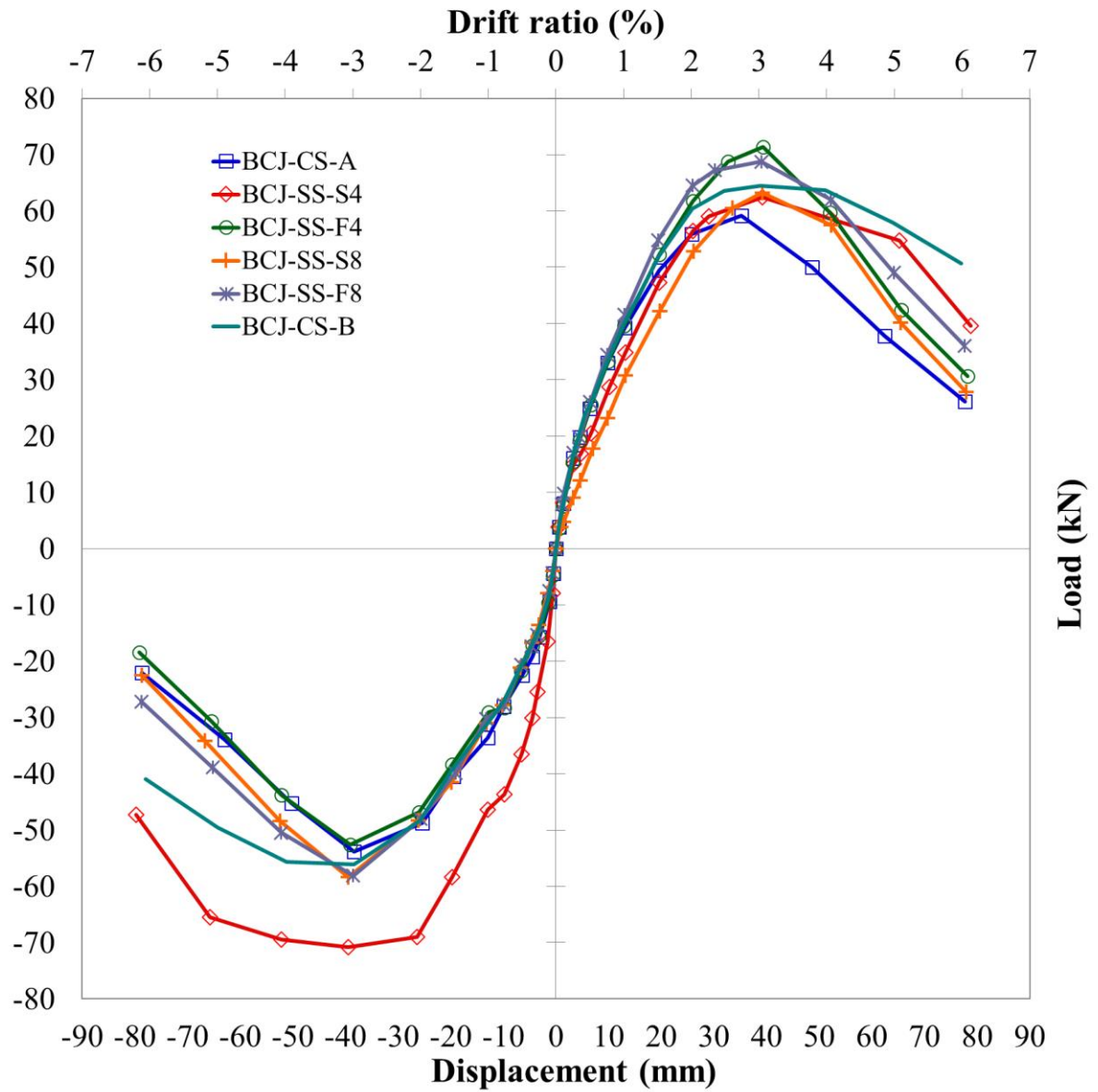
(d) BCJ-SS-S8



(e) BCJ-SS-F8

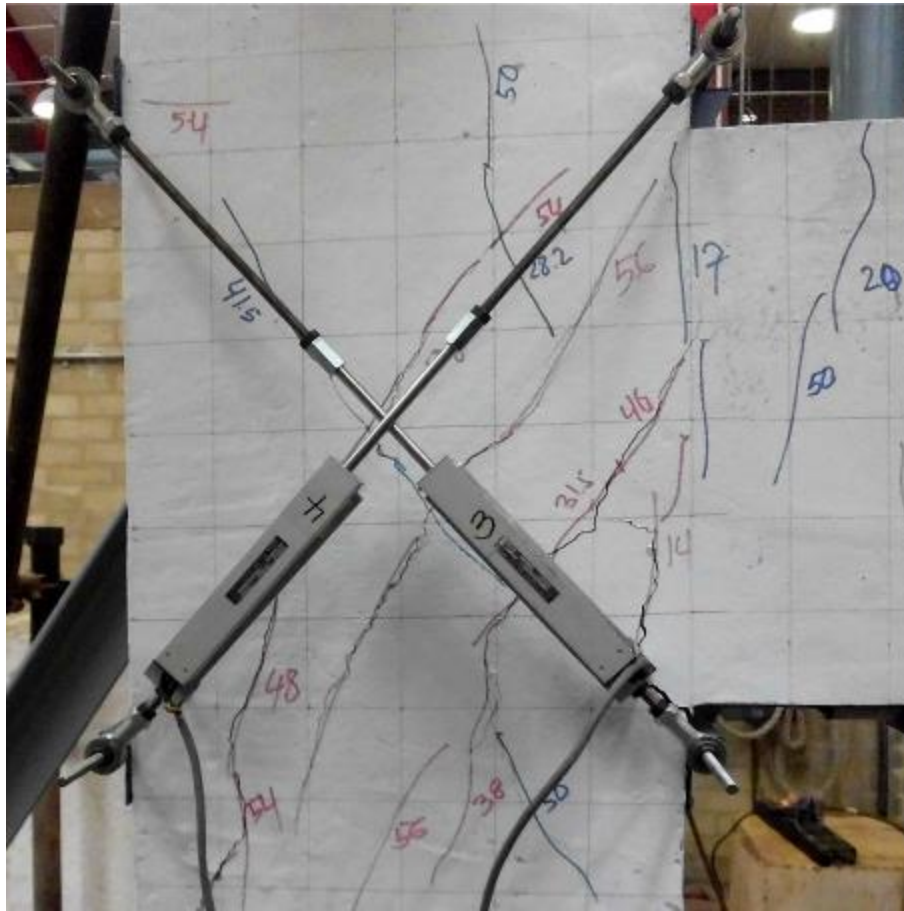


(f) BCJ-CS-B

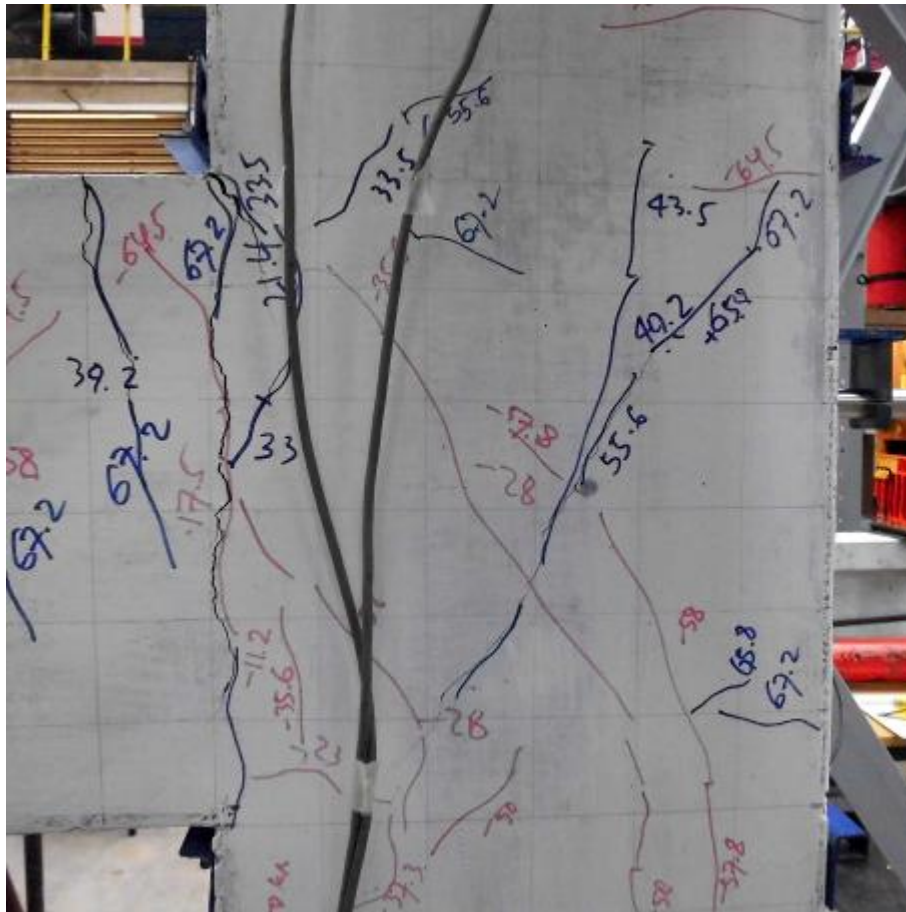


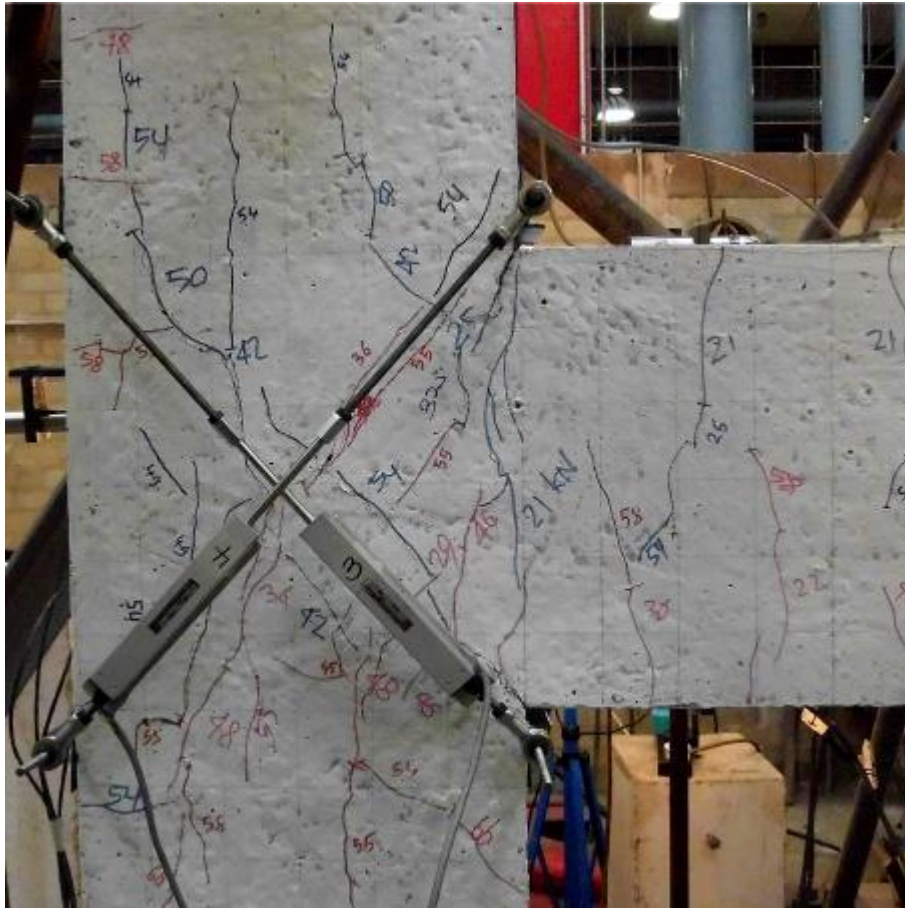
(g) Envelope curves for tested specimens

Fig. 6. Crack patterns of the tested specimens at peak load (corresponding to 3.00% drift ratio).

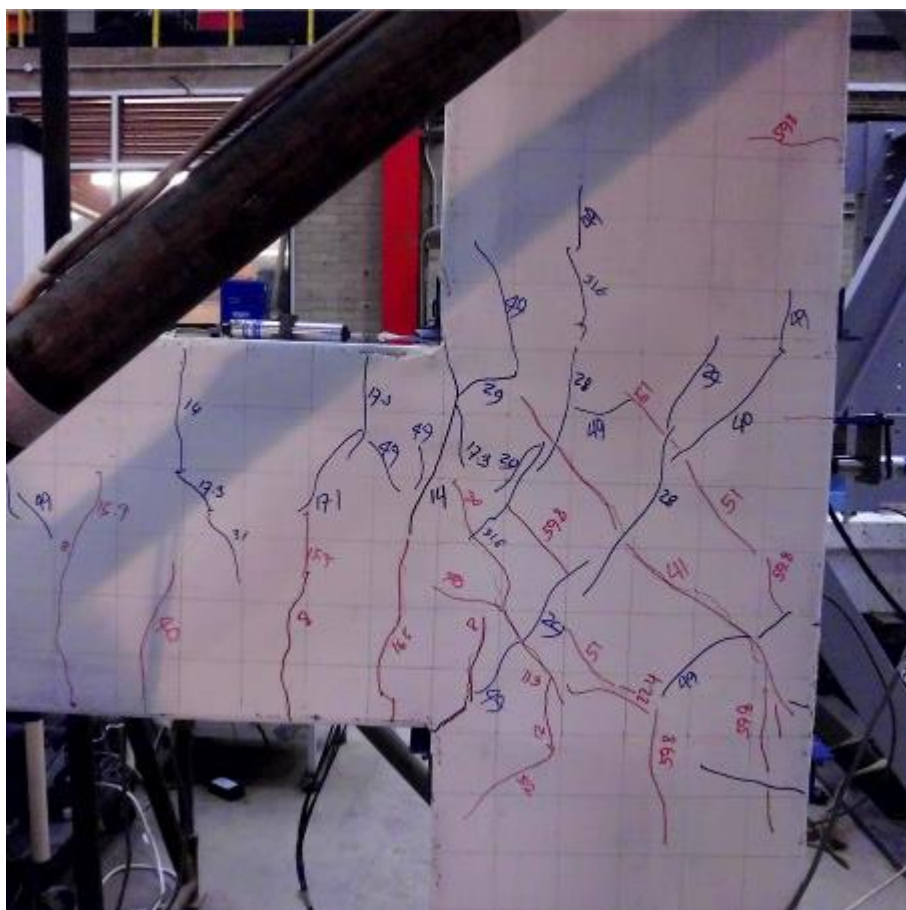


(a) BCJ-CS-A

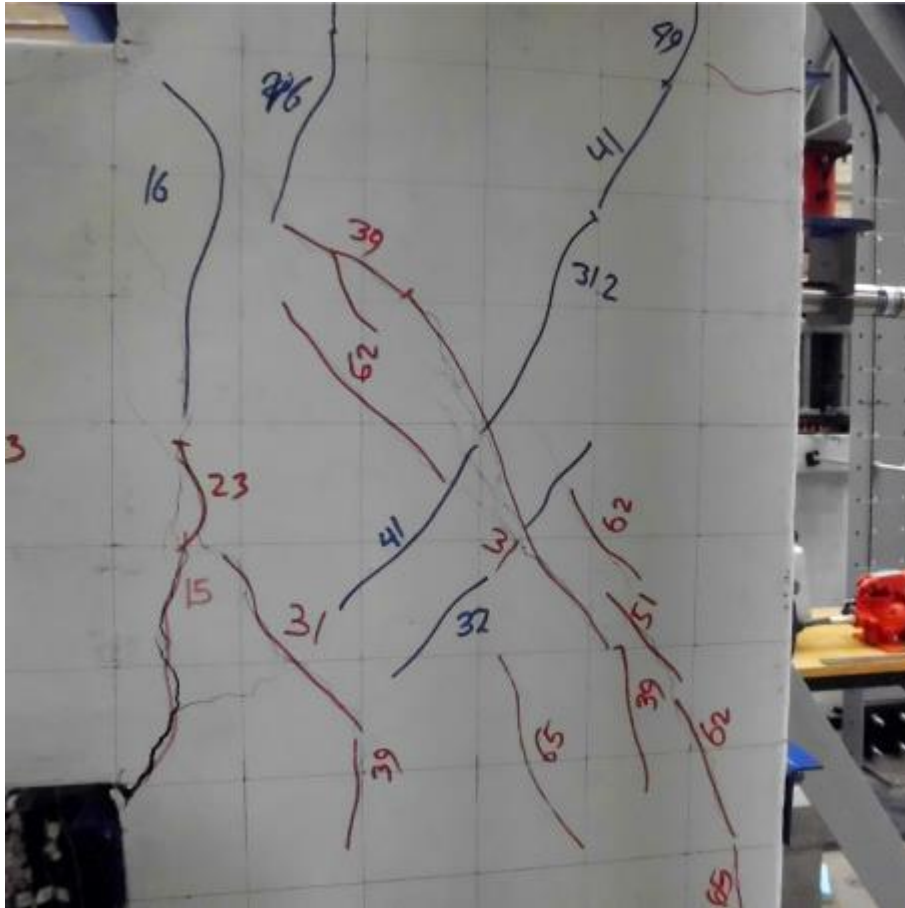




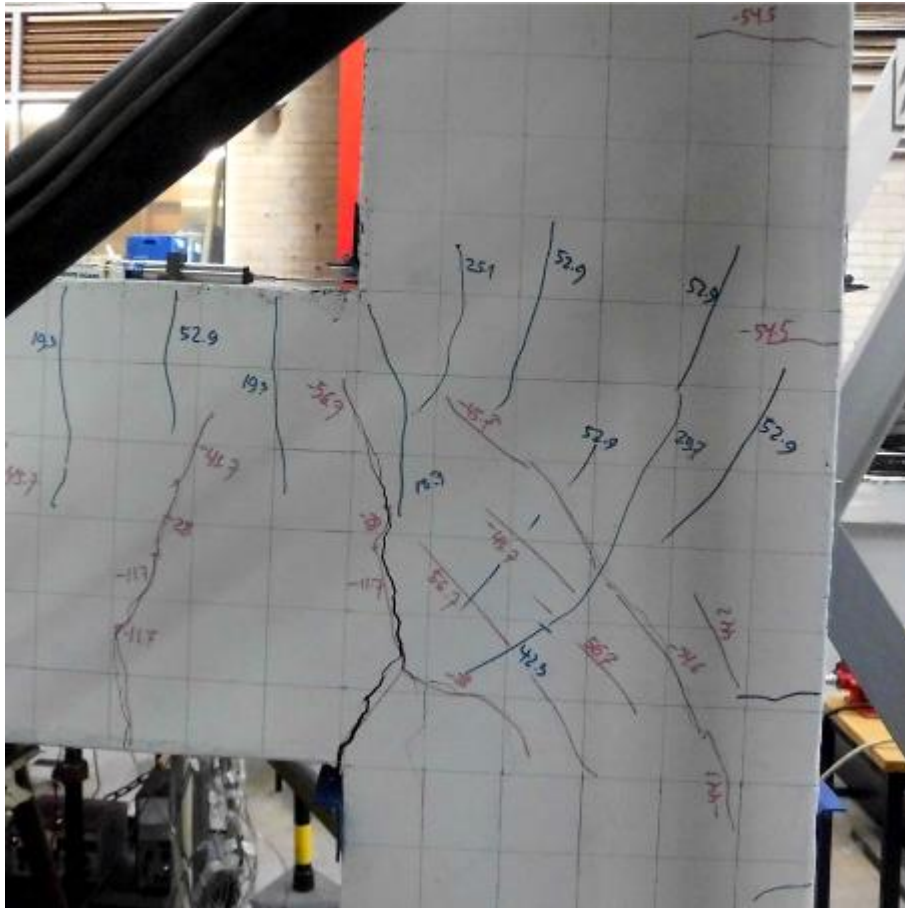
(c) BCI-SS-F4



(d) BCJ-SS-S8



(e) BCJ-SS-F8



(f) BCJ-CS-B

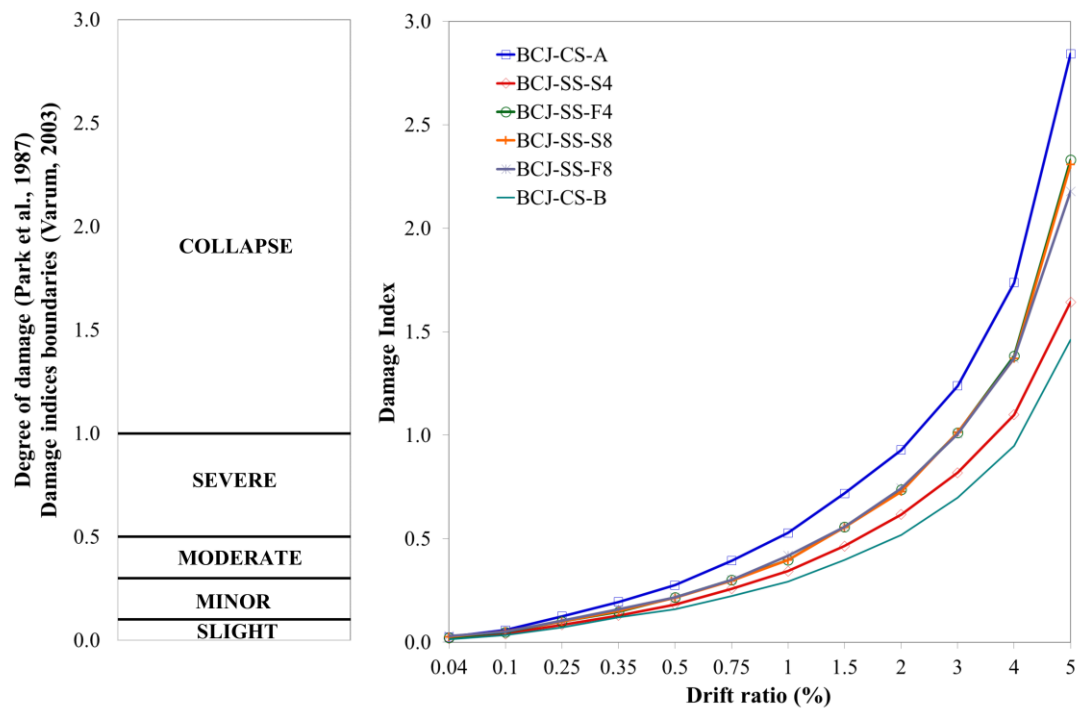


Fig. 7. Damage versus drift ratio.

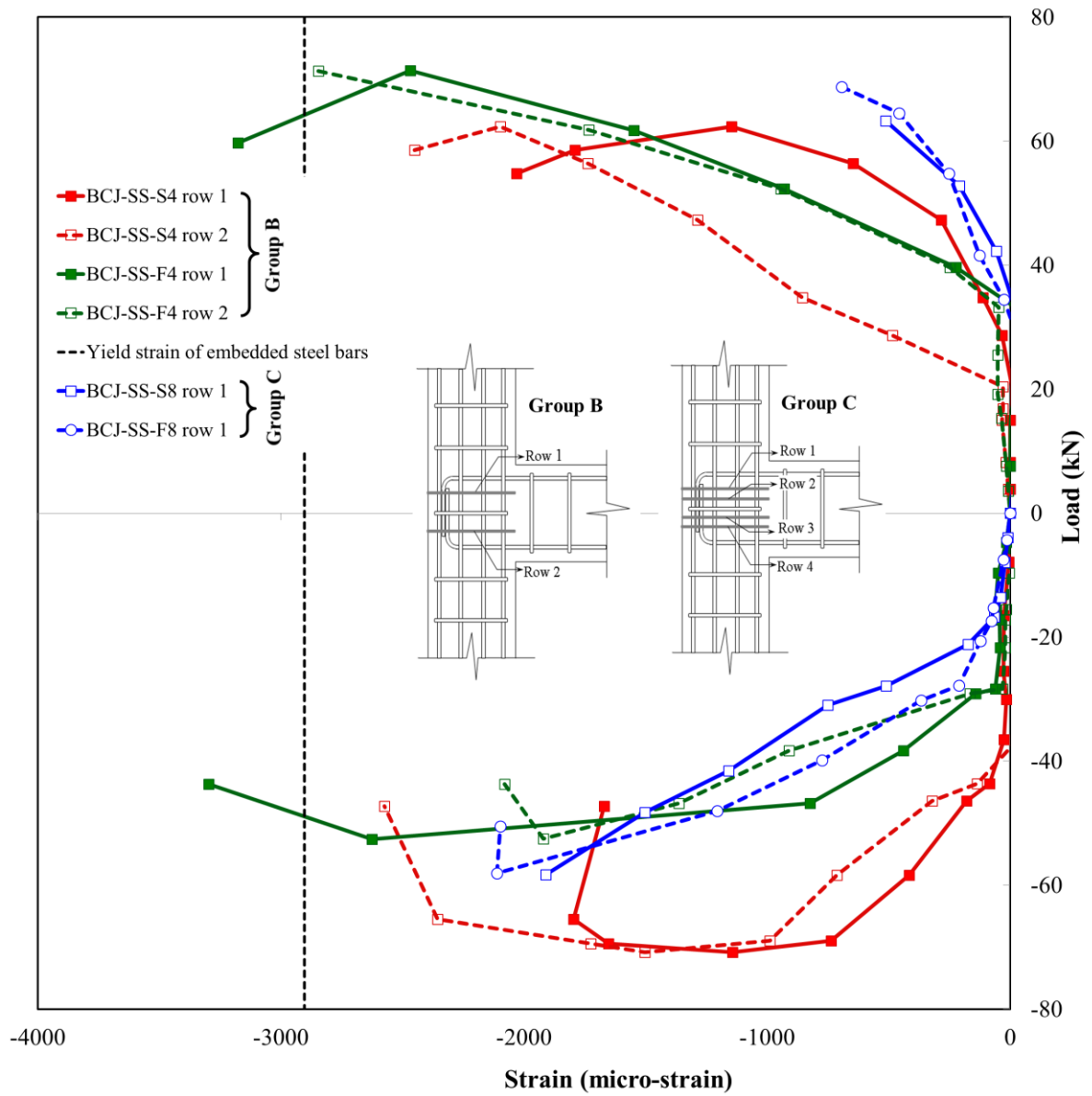


Fig. 8. Envelope curves of load versus strain in the embedded bars.

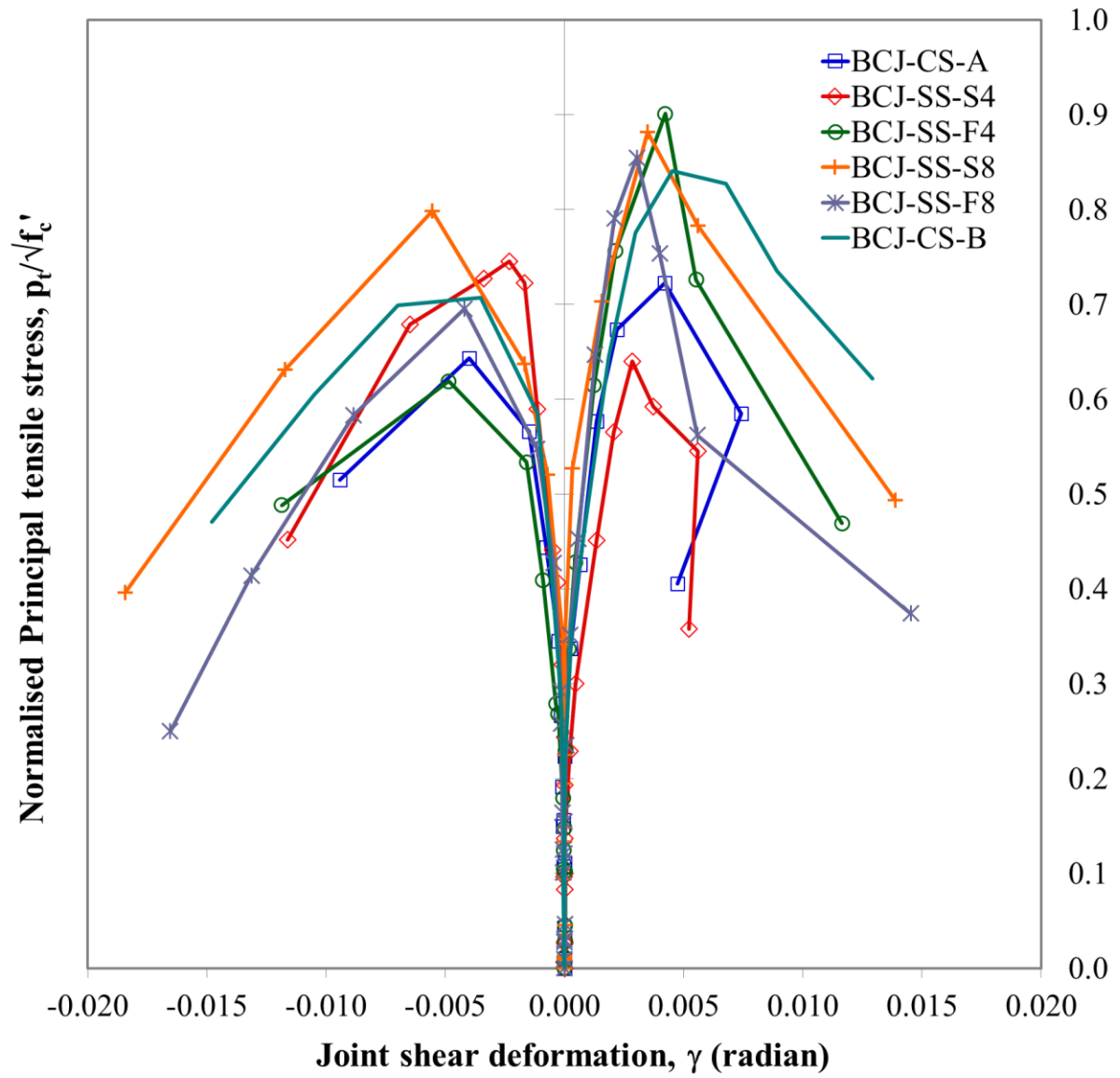


Fig. 9. Envelope curves of normalized principal tensile stress versus joint shear deformation.

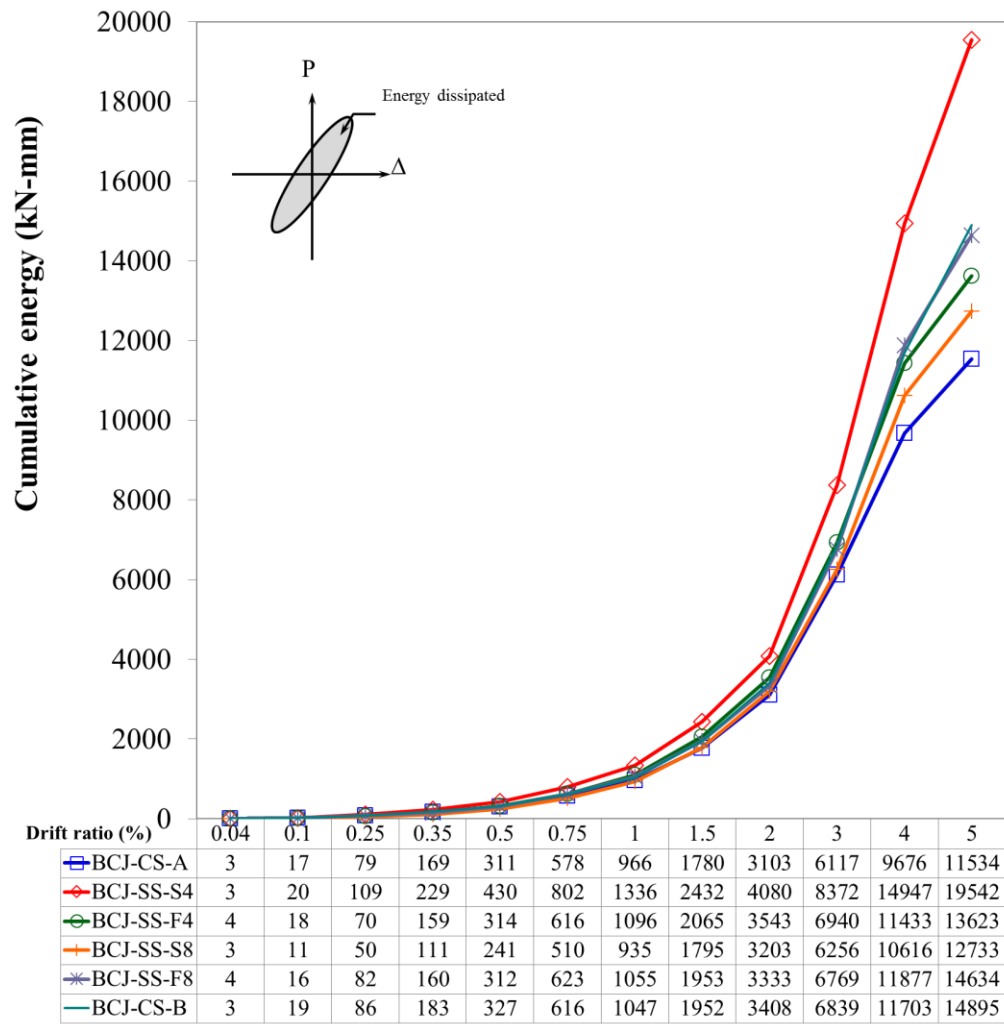


Fig. 10. Comparison of energy dissipation.

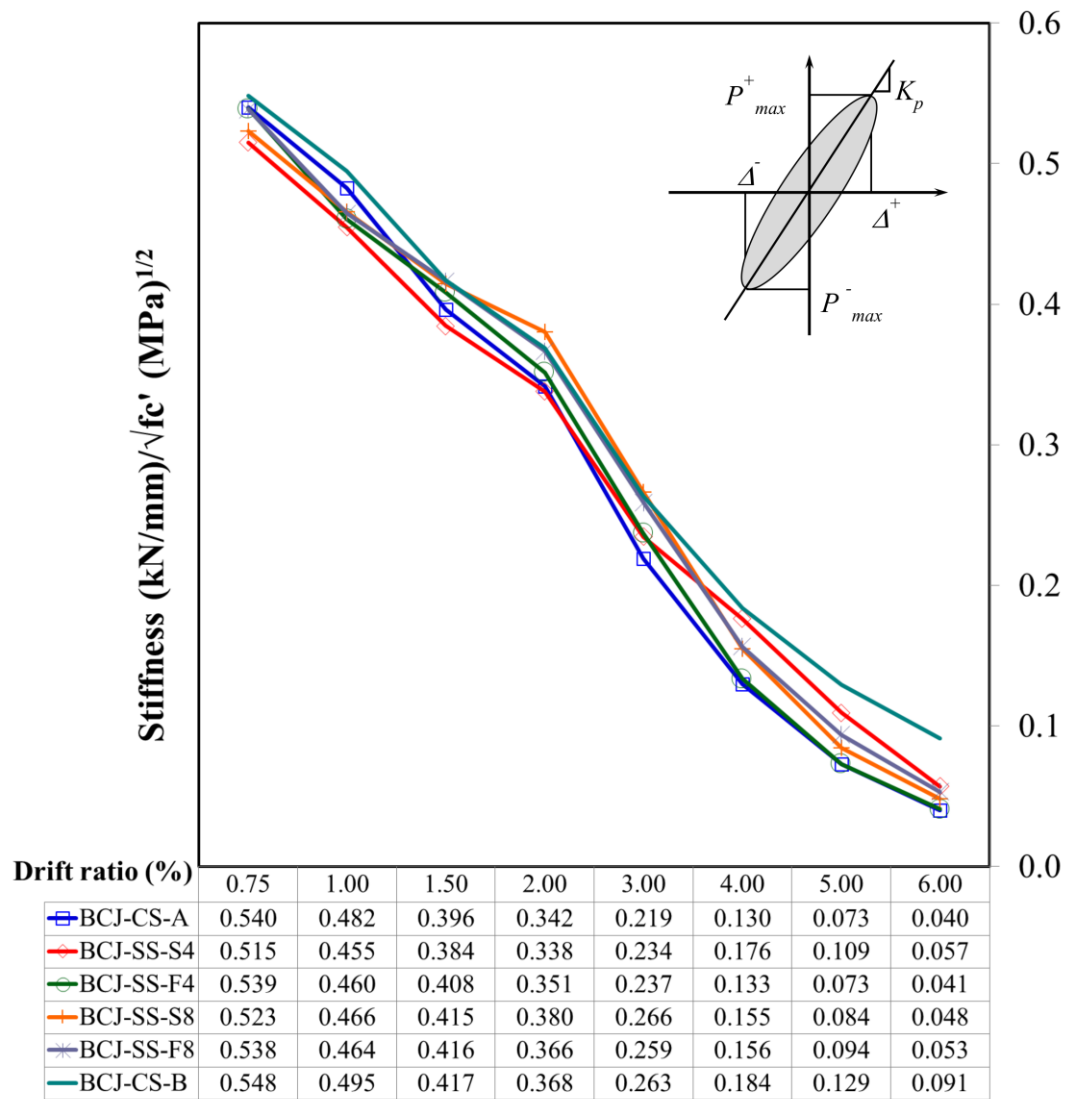


Fig. 11. Comparison of normalized peak-to-peak stiffness.

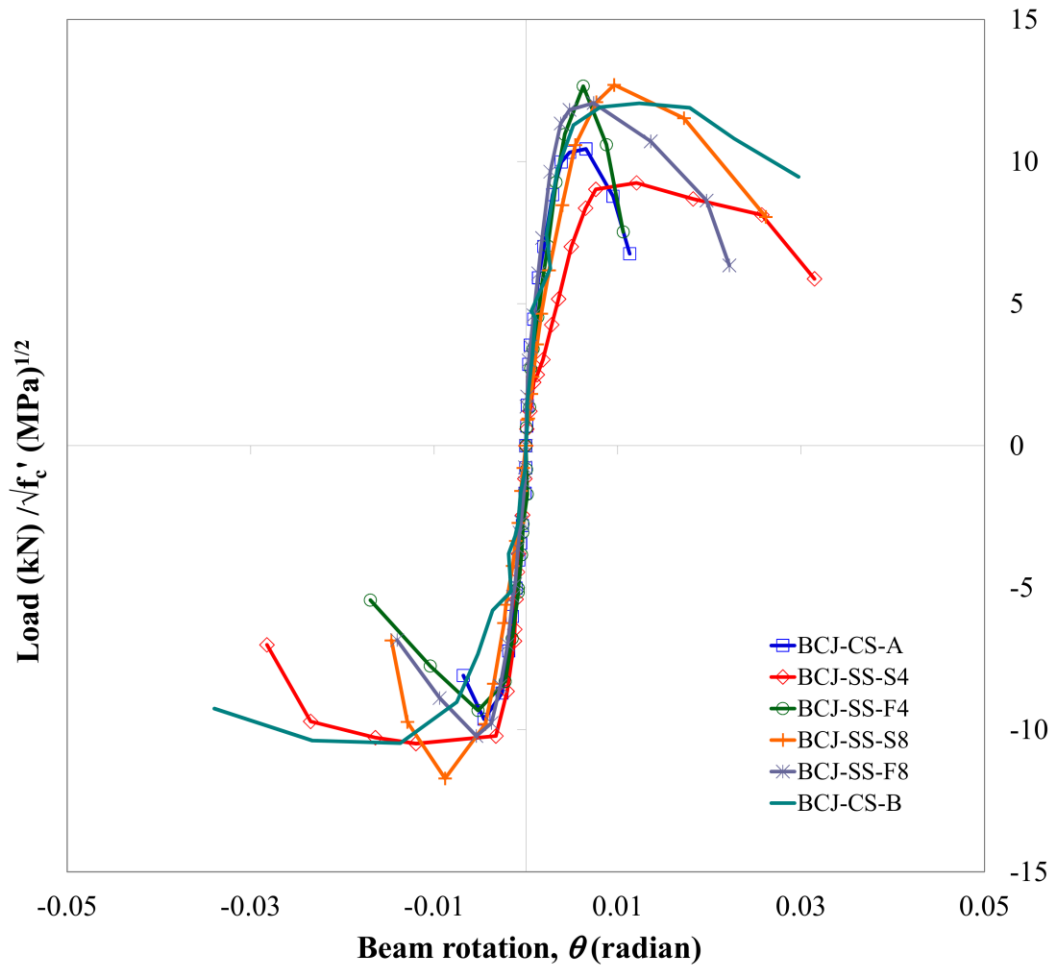
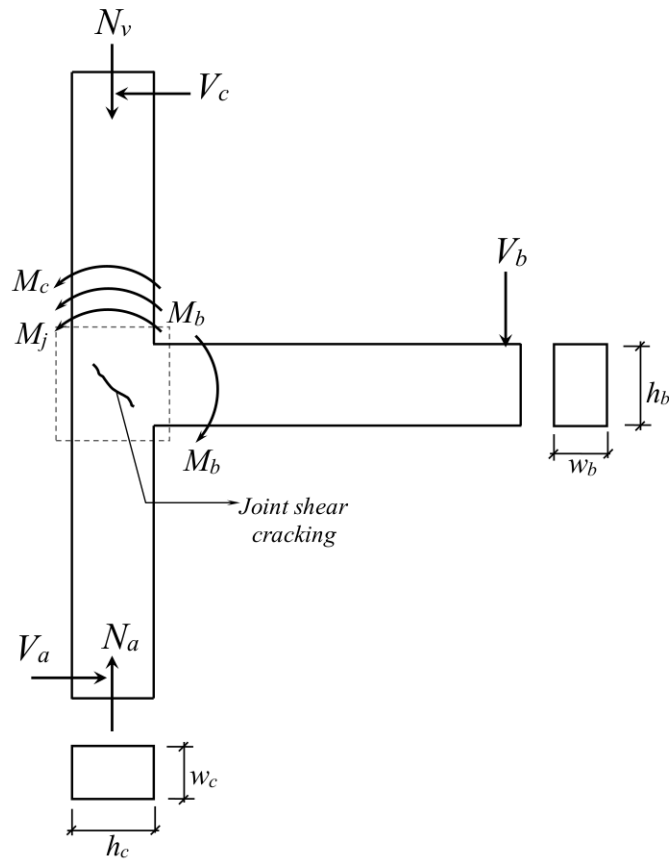
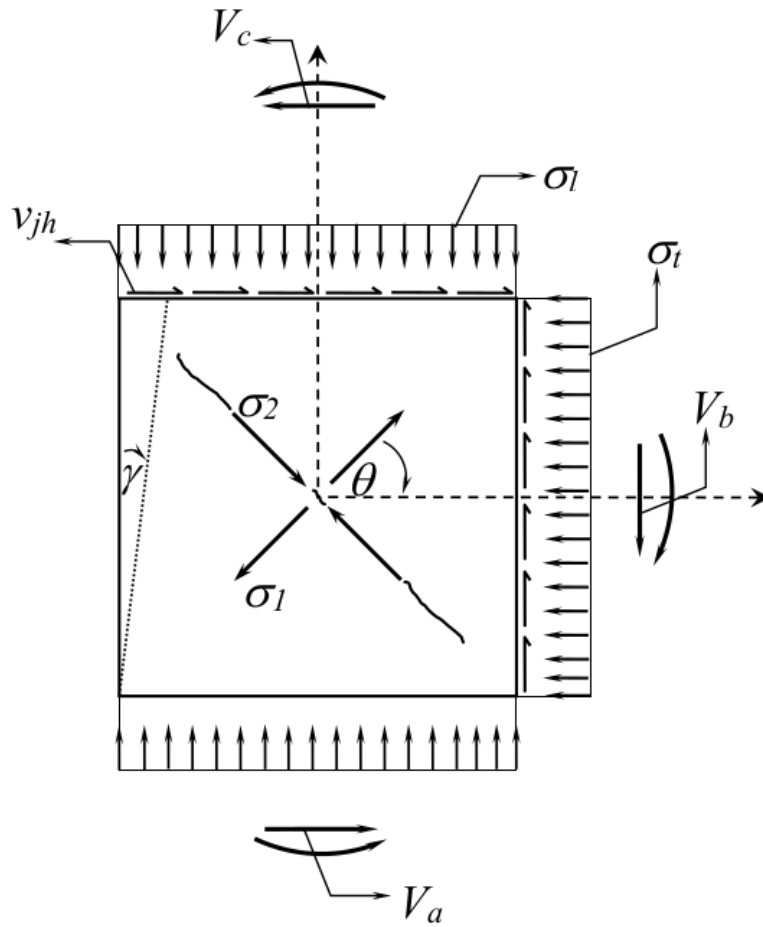


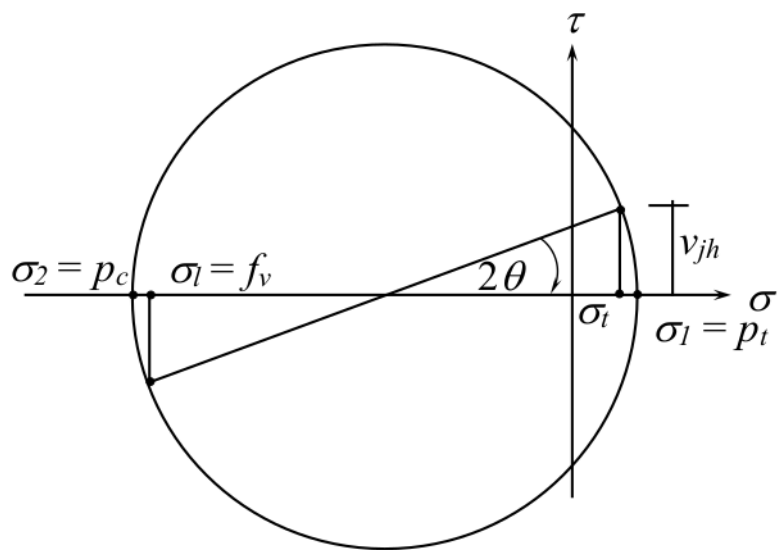
Fig.12. Envelope curves of normalized load versus beam fixed-end rotation.

Fig. 13. Idealization of an external beam-column joint, based on Akguzel and Pampanin (2012).



(a) Moments and shear forces acting on the boundaries of the plane frame element;





1044

1045

1046 (c) Mohr's circle for average stresses.

1047

1048

1049

1050

1051

1052

1053

1054

1055

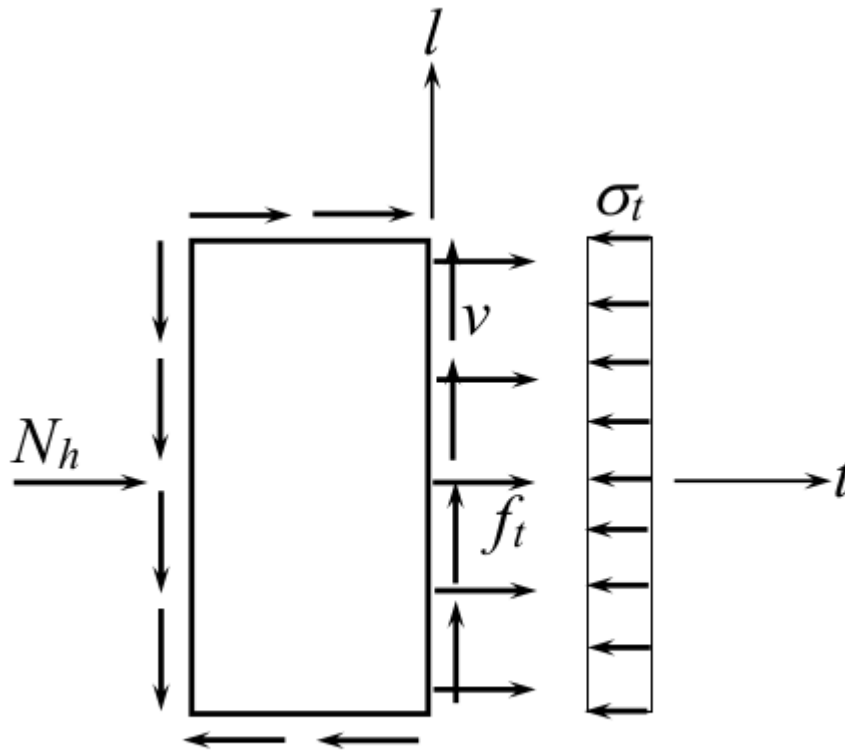
1056

1057

1058

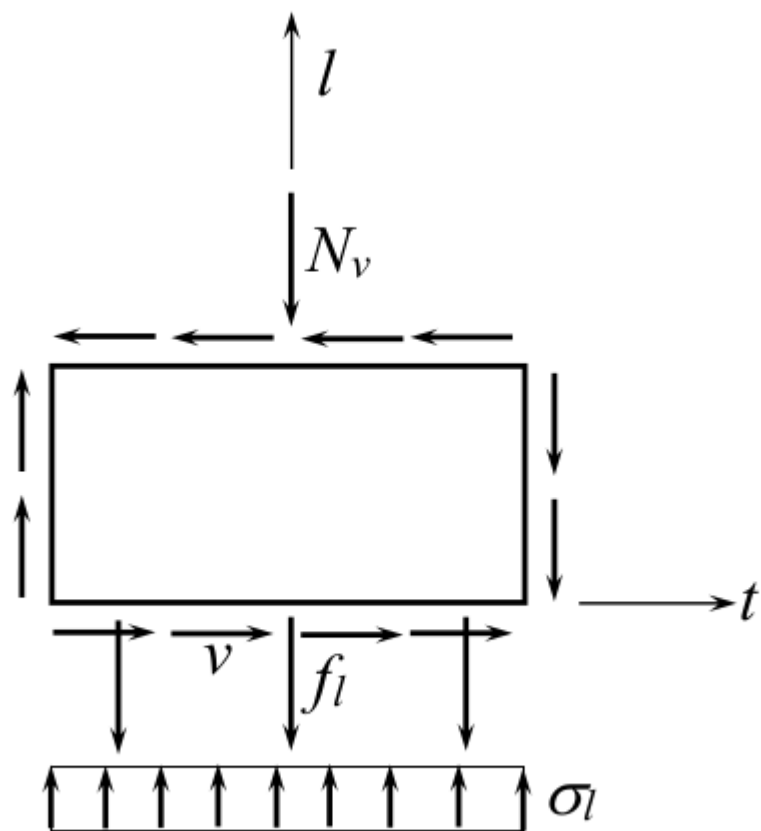
1059

Fig. 14. Stress equilibrium in a joint with embedded bars, modified after Antonopoulos and Triantafillou (2002).



(a) Horizontal forces

1073



1074

1075 (b) Vertical forces

1076

1077

1078

1079

1080

1081

1082

1083

1084

1085

1086 **List of Tables**

1087

1088 Table 1. Details of the tested beam-column joint specimens.

1089 Table 2. Concrete properties.

1090 Table 3. Steel reinforcement properties.

1091 Table 4. Summary of test results.

1092 Table 5. Comparison between experimental and predicted results.

1093

1094

1095

1096

1097

1098

1099

1100

1101

1102

1103

1104

1105

1106

1107

1108

1109

1110

1111 **Table 1.** Details of the tested beam-column joint specimens.

Specimen	Column characteristics			Beam characteristics			Joint	
	Cross-section (mm)	Bars (mm)	Stirrups (mm)	Cross-section (mm)	Bars (mm) (Top and bottom)	Stirrups (mm)	Closed stirrups	Embedded bars
Group A								
BCJ-CS-A							1 Ø8	N/A
Group B								
BCJ-SS-S4	200 × 300	8 Ø16	Ø8@125	200 × 300	3 Ø16	Ø8@125	1 Ø8	4 Ø8 Steel
BCJ-SS-F4							1 Ø8	4 Ø8 CFRP
Group C								
BCJ-SS-S8							1 Ø8	8 Ø8 Steel
BCJ-SS-F8							1 Ø8	8 Ø8 CFRP
Group D								
BCJ-CS-B							5 Ø8	N/A

1112

1113

1114 **Table 2.** Concrete properties.

Specimen	On day of testing	
	f_c (MPa)	f_{ct} (MPa)
BCJ-CS-A	31	3.1
BCJ-SS-S4	45	3.7
BCJ-SS-F4	32	3.3
BCJ-SS-S8	25	2.2
BCJ-SS-F8	32	3.4
BCJ-CS-B	29	2.6

1115

1116

1117 **Table 3.** Steel reinforcement properties.

Bar size (mm)	f_y (MPa)	f_u (MPa)	E_s (MPa)	Remarks
8	581	672	198672	Stirrups and embedded bars
16	512	671	200000	Beam and column longitudinal reinforcement

1118

1119

1120 **Table 4.** Summary of test results.

Specimen	Load Direction	v_{jh}^a (MPa)	p_o/f_c^b	$p_t/\sqrt{f_c}^c$	μ^d	Energy ^e (kN-mm)	Failure Mode
BCJ-CS-A	Upward	5.1	-0.21	0.72	1.8	11534	JS
	Downward	-4.7	-0.19	0.64	1.5		
BCJ-SS-S4	Upward	5.4	-0.15	0.64	2.5	19541	BH
	Downward	-6.2	-0.17	0.75	2.9		
BCJ-SS-F4	Upward	6.2	-0.24	0.90	1.9	13623	BH
	Downward	-4.6	-0.19	0.62	1.9		
BCJ-SS-S8	Upward	5.5	-0.28	0.88	1.7	14056	BH
	Downward	-5.1	-0.26	0.80	1.8		
BCJ-SS-F8	Upward	6.0	-0.23	0.85	2.2	16447	BH
	Downward	-5.1	-0.20	0.70	1.7		
BCJ-CS-B	Upward	5.6	-0.24	0.84	3.3	20233	BH
	Downward	-4.9	-0.22	0.71	2.2		

1121 ^a Horizontal shear stress in the joint at peak load; ^b Normalized principal compressive stress in
 1122 the joint at peak load; ^c Normalized principal tensile stress in the joint at peak load;

1123 ^d Ductility; ^{d,e} Calculated at the loading step corresponding to 20% reduction in ultimate load.

1124

1125

1126 **Table 5.** Comparison between experimental and predicted results.

Specimen	Joint shear strength (MPa)		Predicted/ Experimental ratio
	Experimental	Predicted	
BCJ-CS-A	5.1	5.2	1.01
BCJ-SS-S4	5.4	5.6	1.03
BCJ-SS-F4	6.2	6.5	1.04
BCJ-SS-S8	5.5	5.9	1.07
BCJ-SS-F8	6.0	6.1	1.02
BCJ-CS-B	5.6	6.2	1.11
Average			1.05
Standard deviation			0.04

1127